GCAGS JOURNAL
A Publication of the Gulf Coast Association of Geological Societies
www.gcags.org

Depositional Systems, Lithofacies, Nanopore to Micropore Matrix Network, and Reservoir Quality of the Upper Cretaceous (Cenomanian) Buda Limestone in Dimmit County, Southwestern Texas

Robert G. Loucks[1], Bruce G. Gates[2], and Christopher K. Zahm[1]

[1]*Bureau of Economic Geology, Jackson School of Geosciences, University of Texas at Austin, University Station, Box X, Austin, Texas 78713–8924, U.S.A.*

[2]*Ageron Energy, LLC, 1250 NE Loop, Ste. 500, San Antonio, Texas 78729, U.S.A.*

ABSTRACT

The Upper Cretaceous Buda Limestone is a well-explored fractured reservoir in South Texas. It is composed of highly burrowed, calcisphere–planktic foraminifer lime wackestones and some packstones with a coccolith-hash matrix. The depositional setting is interpreted to be a deeper water, below-storm-wave-base, quiet-water, aerobic environment. The dominance of planktic biotas with rare benthic biotas, along with abundant bioturbation, is evidence of this setting. The full Buda section is composed of alternating in-place strata and thick-bedded mudflows of resedimented deepwater material with abundant soft-sediment clasts. The major hydrocarbon producing pore network is composed of fractures. Evidence of larger scale fractures commonly associated with faults and flexures were not noted in the two cores investigated, but many smaller, calcite-filled fractures related to chemical (solution seams) and mechanical compaction were noted. Matrix pores consist of interparticle nanopores to micropores between coccolith hash. The original pores have been partly to totally occluded by calcite overgrowth cement. Porosity ranges from 1 to 5%, and permeability is generally less than 0.1 md. Pore throats range from 5 to 200 nm. It is speculated that even though hydrocarbon production depends on fractures, the matrix may contribute some hydrocarbons, especially into the large widespread flat conduits created by the fractures.

INTRODUCTION

The Upper Cretaceous (Cenomanian) Buda Limestone on the South Texas drowned Lower Cretaceous shelf (Figs. 1 and 2) is a well-explored fractured chalky reservoir that has been under hydrocarbon production since early 1900s (e.g., Dawson, 1986; Petzet, 1990; Darbonne, 2012; Davis et al., 2016). Several studies have described the basic lithofacies (e.g., Hixon, 1959; Erdogan, 1969; Reaser and Dawson, 1995; Ak, 2015; Hendrix, 2016), some have investigated the origin of fractures and their distribution (e.g., Snyder and Craft, 1977; Stapp, 1977; Parker, 2000; Smirnov and Liner, 2018), and others have emphasized hydrocarbon exploration and production (e.g., Scott, 1977; Dawson, 1986). Very little research effort, however, has addressed the depositional processes that deposited the Buda sediments or the pore networks within the matrix. Two long cores (Figs. 1 and 3–6) from Dimmit County in South Texas display the Buda Limestone, and both cores capture the Del Rio Formation contact below and the Eagle Ford Group contact above (Fig. 6). The analysis of these cores allows a detailed geologic characterization of the complete Buda Limestone in southwestern Texas.

Specific objectives of this research effort are to (1) describe the lithofacies within the Buda Limestone and associated depositional processes that deposited the original sediments, (2) define the pore types identified in cores and explain how they evolved with burial, and (3) discuss the reservoir quality of the Buda Limestone matrix through analysis and integration of core-plug porosity and permeability and high-pressure mercury injection capillary pressure (MICP). The completion of these objectives provides a detailed analysis of the deposition of the Buda Limestone in southwestern Texas. Also, scanning electron microscope analysis of the carbonate clay- to very fine silt-sized grains and the nanopore to micropore network adds understanding of potential hydrocarbon contribution from matrix pores.

Copyright © 2019. Gulf Coast Association of Geological Societies. All rights reserved.

Manuscript received February 6, 2019; revised manuscript received May 9, 2019; manuscript accepted June 6, 2019.

GCAGS Journal, v. 8 (2019), p. 281–300.
DOI: pending

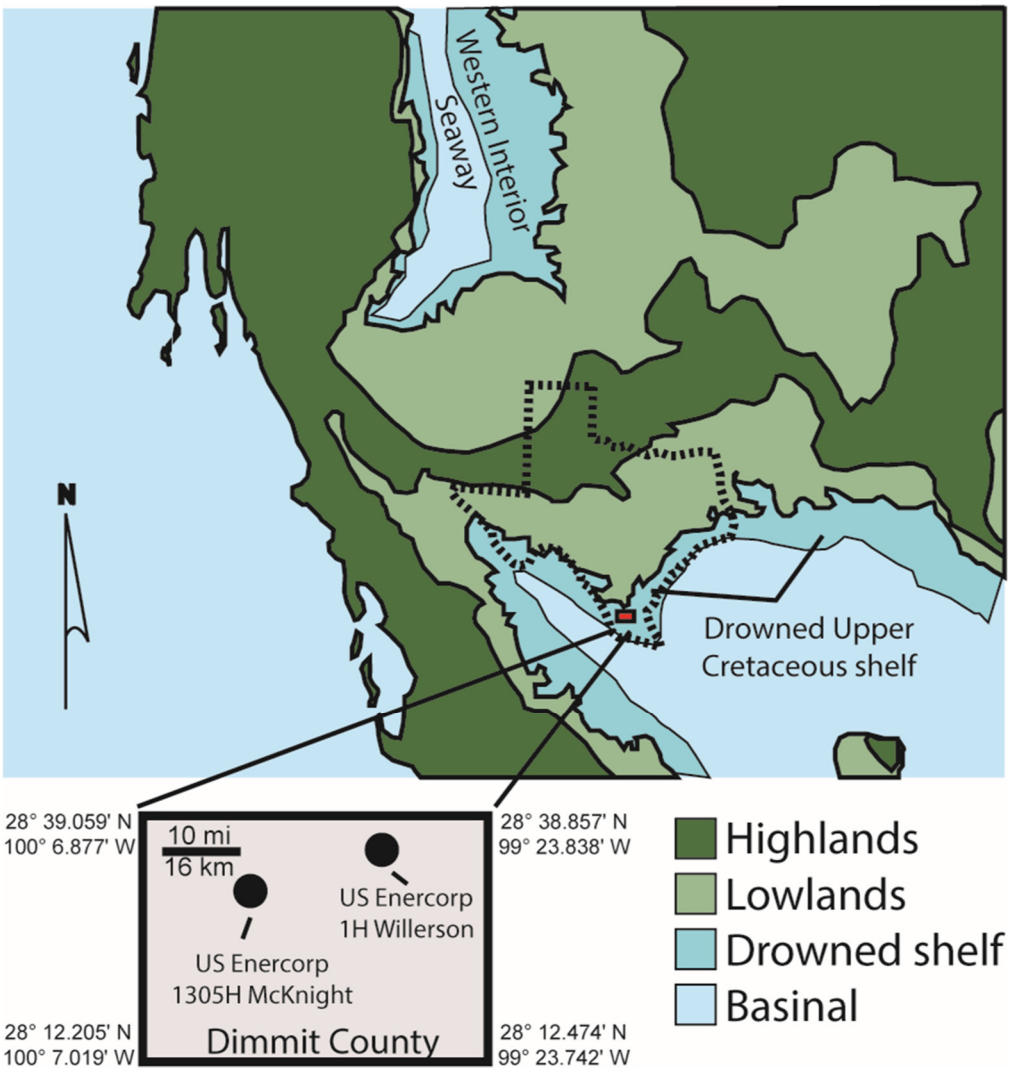

Figure 1. Regional depositional setting and location of studied cores. The Buda Limestone was deposited on the drowned South Texas Lower Cretaceous shelf during the early Cenomanian. General land masses. Map is modified after Blakey (2016).

DATA AND METHODS

Two cores within Dimmit County (Figs. 1, 3, and 5) are the basic data for this investigation: the US Enercorp 1H Willerson (7054 to 7218 ft [2151 to 2200 m]) and the US Enercorp 1305H McKnight (5667 to 5829 ft [1727 to 1777 m]). Wireline log suites are available for both cores (Fig. 6).

The cores were slabbed and lightly etched with dilute HCl to bring out rock texture and to cause insoluble minerals to stand in very slight relief. They were then described with a binocular microscope with the aid of associated thin sections. Photographs of each core box were taken in both plain light and ultraviolet (UV) light. Numerous individual core slabs were photographed as a method of documenting lithofacies and fabrics. Approximately 300 thin sections were investigated. Each thin section was impregnated with blue epoxy to highlight macropores and with blue-fluorescent dye to highlight nanopores and micropores (using mercury-vapor light).

Routine core analysis for porosity and permeability was run on 330 1 in (2.54 cm) core plugs by Weatherford Laboratories (Houston, Texas) and POROLABS (Houston, Texas). The samples were extracted of any liquids using Dean-Stark procedures. The samples were tested at 800 psi (5.52 MPa) overburden pressure for the 1305H McKnight core and at 2250 psi (15.51 MPa) for the 1H Willerson core. Porosity values were calculated using the measured grain volume and pore volume data. Permeability was calculated using unsteady-state flow equations and Klinkenberg corrected. Plug measurement with notations that the plugs were fractured were omitted from any tabulations. Thirty-six high-pressure MICP analyses were conducted on fresh core plugs by POROLABS. Samples were subjected to pressures as high as 60,000 psi (413.7 MPa).

Selected samples from several lithofacies in the 1H Willerson well were viewed on a field-emission scanning electron microscope (FESEM) with an energy-dispersive X–ray spectrometer (EDS) to characterize detailed biotas, mineralogy, crystal morphology, diagenetic features, and pores. Two types of samples were viewed: (1) rock chips to characterize biota, crystal morphology, and diagenetic features in three dimensions and (2) Ar–ion-milled samples (see Loucks et al. [2009] for review) to analyze a flat surface that allows two-dimensional as well as limited three-dimensional viewing of areas where pore space exists. The samples were observed using the FEI Nova NanoSEM 430 at the University of Texas at Austin. Use of this FESEM equipped with in-lens secondary electron detectors provided greatly enhanced detail of nanometer-scale features. Lower accelerating voltages (10–15 kV) were generally used on these samples to prevent beam damage, and working distances were 0.118 to 0.354 in (3 to 9 mm).

A handheld microrebound hammer was used to characterize rock strength (unconfined compressive strength [UCS]) in both cores following the method developed by Zahm and Enderlin (2010). Sampling was done at a spacing of 2 to 4 in (5 to 10 cm), depending on the condition of individual core slabs.

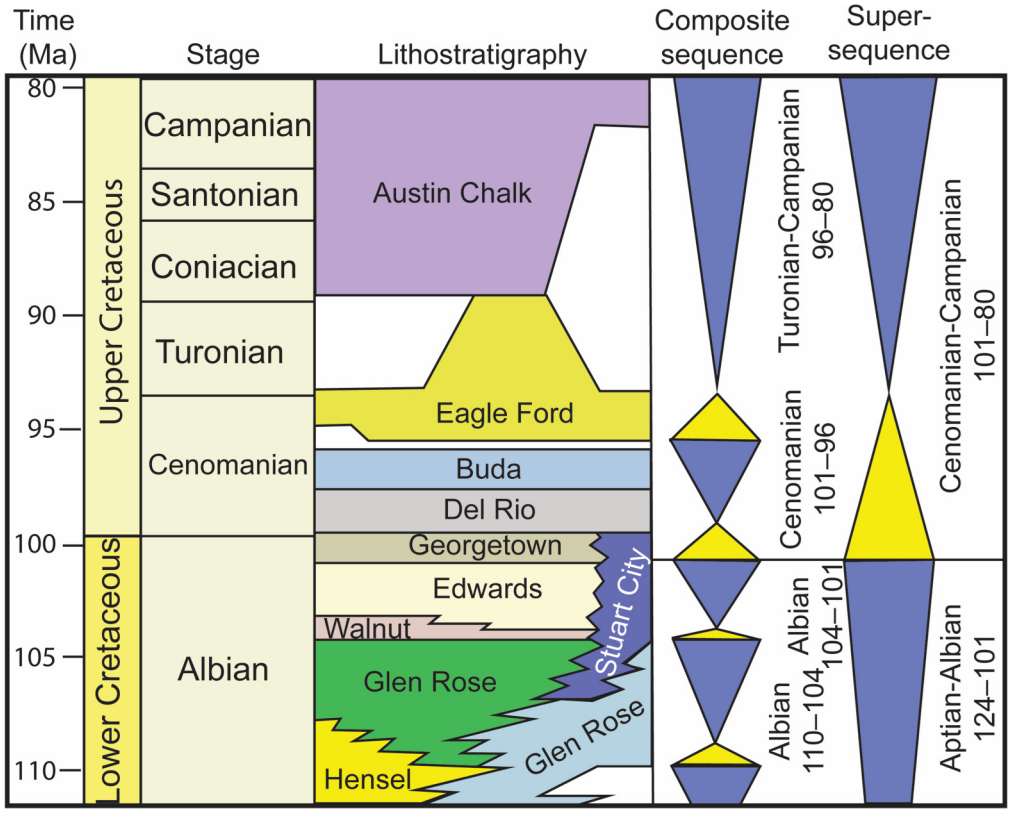

Figure 2. General stratigraphic section for the South Texas shelf area (modified after Phelps et al., 2013).

REGIONAL GEOLOGIC SETTING AND GENERAL STRATIGRAPHY

The Buda Limestone was deposited on the broad, drowned Lower Cretaceous shelf, and the study area is approximately 30 mi (48 km) to the north behind the raised paleo–Stuart City shelf margin and is on the southern rim of the Maverick intrashelf basin.

Phelps et al. (2013) designated the Del Rio and Buda formations to be in the regressive leg of the Cenomanian 101–96 Ma composite sequence, but at a longer-term scale to be in the transgressive leg (overall deepening) of the Cenomanian–Campanian 101–80 Ma supersequence (Fig. 2). Overall, from the beginning of the Del Rio deposition through the early Eagle Ford Group there was a long-term sea-level rise on the South Texas carbonate platform.

Phelps et al. (2013) noted that the drowning of the Albian Stuart City reef margin occurred during the early Cenomanian with deposition of the Del Rio Formation. These sediments began filling the accommodation that was created by the differential shelf to Stuart City barrier-reef-complex topography. The updip Del Rio siliciclastic sediments were deposited in a brackish to marine depositional setting (Butler, 2009; Lock et al., 2009), whereas downdip, equivalent normal marine carbonates were deposited (Alnahwi et al., 2018; this study).

Following deposition of the Del Rio Formation, the middle Cenomanian (Denne et al., 2016) carbonate Buda Limestone was deposited and continued filling the depositional low on the drowned shelf. The Buda Limestone is the first of a series of deeper water chalk (coccolith-hash-dominated matrix) units deposited during the Late Cretaceous on the drowned Lower Cretaceous paleoshelf. In the updip area, the Buda is in erosional contact with the Del Rio Formation below (Lock et al., 2009). Just west of Del Rio, Texas, large (up to 2 ft [0.6 m]) carbonate and sandstone lithoclasts are found in the first few feet of the lowermost Buda section. Downdip, in the area of this study, the contact appears gradational, as seen in core and on wireline logs (Figs. 3, 5, and 6). Both Lock et al. (2007) and Donovan et al. (2012) concluded that the contact between the Del Rio and Buda Formations is a third-order sequence boundary.

The middle Cenomanian to upper Turonian Eagle Ford Group has a sharp, erosional contact with the lower Cenomanian Buda Limestone below, as seen in many cores on the South Texas shelf by the senior author of this present investigation. Also, Loucks (2018) interpreted that the surface between the Buda and the Eagle Ford section west of Del Rio, Texas, is a submarine unconformity and is marked by an irregular pitted solution surface that appears to have been well lithified before deposition of Eagle Ford strata. Some Buda lithoclasts are present just above the contact. Wireline logs also show a very sharp contact going from the Buda cleaner carbonates below to very argillaceous Eagle Ford mudstones above. As noted earlier, Phelps et al. (2013) assigned this surface as the contact between two composite sequences (Fig. 2). The change from Buda strata to lower Eagle Ford strata is also marked by a sharp increase in total organic content: generally from less than 0.3 wt% to more than 2.0 wt% (based on data collected by senior author).

LITHOFACIES

The cores used in this investigation recovered material from the Del Rio, Buda, and Eagle Ford units. In the following subsections, lithofacies in each unit are described, and photographs of samples are provided.

Del Rio Formation

In the 1H Willerson core, 7 ft (2.1 m) of the Del Rio section was recovered, and 5 ft (1.5 m) was recovered in the 1305H McKnight core (Figs. 3, 5, and 7A–7D). The short-cored sections consist of horizontally burrowed, argillaceous and dolomitic lime mudstone and horizontally to vertically burrowed, argillaceous skeletal lime wackestone to packstone. Thin argilla-

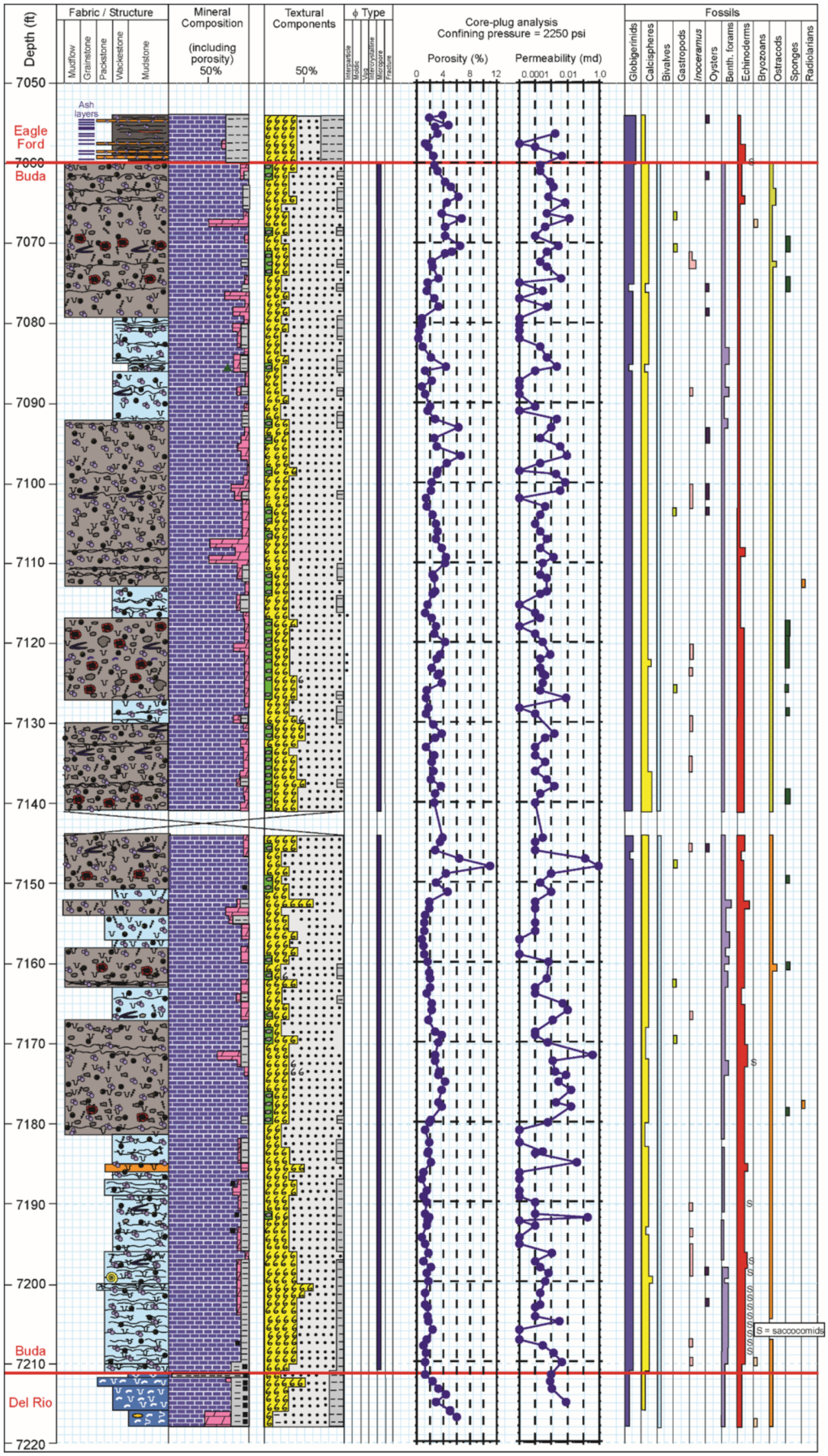

Figure 3. US Enercorp 1H Willerson core description. Porosity and permeability values are from routine core-plug analysis. American Petroleum Institute (API) number = 4212735690000. Core symbol legend shown in Figure 4.

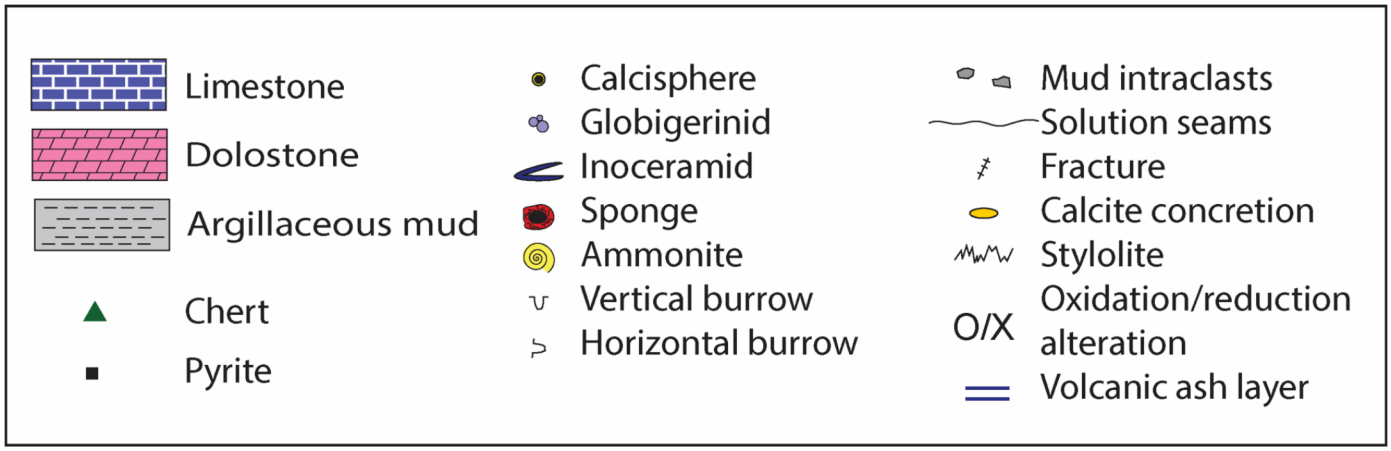

Figure 4. Legend for core descriptions shown in Figures 3 and 5.

ceous mudstones or shales occur in the upper Del Rio cored section (Fig. 7D). Allochems include planktic foraminifers (globigerinids), calcispheres, bivalves, benthic foraminifers, echinoderms, and ostracods. Pyrite nodules (Fig. 7B) and pyritized fossils are common in these Del Rio strata.

These strata suggest a deeper water, below-storm-wave-base, oxygenated setting on the drowned outer shelf. Pelagic biotas supplied the major portion of the sediment by suspension. The vertical burrows in the wackestones and packstones indicate oxygenated sediments that allowed deeper burrowing, whereas the horizontal burrows in the mudstone suggest more stressed or lower oxygenated conditions within the sediments.

Buda Limestone

The complete sections of the Buda Formation were acquired in the 1H Willerson (151 ft [45.0 m]) (Fig. 3) and 1305H McKnight (159 ft [48.4 m]) wells (Fig. 5). The sections are predominantly burrowed, calcisphere globigerinid lime wackestones and packstones with multiple compacted layers of argillaceous limestone (Figs. 8–11). Other allochems include bivalves, rare gastropods, inoceramid fragments (Fig. 9B), oyster fragments, benthic foraminifers (Fig. 9C), saccocomid fragments (Figs. 9A and 9B), sponges (Fig. 8H), and radiolarians (Fig. 9C). Some of the wackestones are nearly homogenous because of burrowing activity (Fig. 8A). Most burrows are vertical *Thalassinoides* in the lime matrix (Fig. 8B) and horizonal *Planolites* in the argillaceous seams (Figs. 8C and 8D). Some of the argillaceous seams and burrows near the top of the Buda Limestone section (just below the Eagle Ford Group) fluoresce under UV light (Fig. 11). The fluorescence may be caused by altered volcanic ash material. This interpretation is based on the fact that the volcanic ash layers in the Eagle Ford Group above fluoresce (Fig. 11). The argillaceous zones show strong compaction and pressure solution (Figs. 8C and 8D). The lime mud (much of which is coccolith hash [Fig. 10]) was deposited by suspension and reworked by bottom currents and bioturbation.

The argillaceous material is interpreted to be associated with hyperpycnal storm-return currents. This argillaceous material filled burrows in firmgrounds that formed at short-term hiatuses (Fig. 8B). The mineralogy of the cleaner wackestones and packstones is calcite. Dolomite crystals (Fig. 9E) and quartz silt are common in the argillaceous seams.

Some of the coccolith-rich sediments was resedimented by mudflows (Figs. 3, 5, 8F–8H, and 11). The mudflows are darker and commonly contain soft-mud rip-up intraclasts (Figs. 8F and 8G) and sponge fragments (Fig. 8H).

One 13 ft (4 m) section in the 1305H McKnight core (5688 to 5711 ft [1733.7 to 1740.7 m]) has oxidization/reduction alteration rims (Fig. 8E) around burrows. Because of the deeper water origin of the Buda sediments, these oxidization/reduction alteration rims cannot be associated with subaerial exposure. They are interpreted to be formed at a long-lived hiatus where oxygen-rich water circulated through the burrow system.

Eagle Ford Group

In the 1H Willerson well (Fig. 3), 6 ft (1.8 m) of the basal Eagle Group was cored, and 3 ft (0.91 m) was cored in the 1305H McKnight well (Fig. 5). The section is composed predominantly of laminated, organic-rich, highly argillaceous lime wackestone having multiple interbeds of transported less argillaceous lime packstone and at least 12 thin (millimeter to centimeter) volcanic ash beds (Figs. 7E–7H and 11). Coccolith hash, planktic foraminifers (globigerinids), and calcispheres predominate as the major allochems, but some saccocomids (floating crinoids) are also present.

The planktic biotas, laminations, and lack of any bioturbation suggest a deepwater, anaerobic depositional setting below storm-wave base. The thin packstone layers are probably related to bottom currents or dilute gravity flows redepositing chalky oozes from updip.

BUDA DEPOSITIONAL MODEL

A series of depositional models are presented for the Buda Limestone (Fig. 12). On the basis of an original sediment mixture of planktic biotas, especially coccolith hash, calcispheres, and planktic foraminifers, and benthic biotas and abundance of deep-sediment bioturbation, Buda sedimentation is interpreted to have occurred in a moderate-water-depth (below-storm-wave-base), aerobic, quiet-water (except for periodic gravity flows) depositional setting.

Three basic process-related facies are present in the Buda section in the study area: (1) in-place deposits reflecting suspension sedimentation (Fig. 12A), (2) periodic storm-return deposits (Fig. 12B), and (3) mudflows (mudflow resedimentation) (Fig. 12C). Both cores display these three process-related facies.

In-Place and Storm-Return Sedimentation

In-place sedimentation (Fig. 12A) is characterized by the accumulation of pelagic sediments, including coccolith hash, planktic foraminifers, calcispheres, saccocomids, radiolarians,

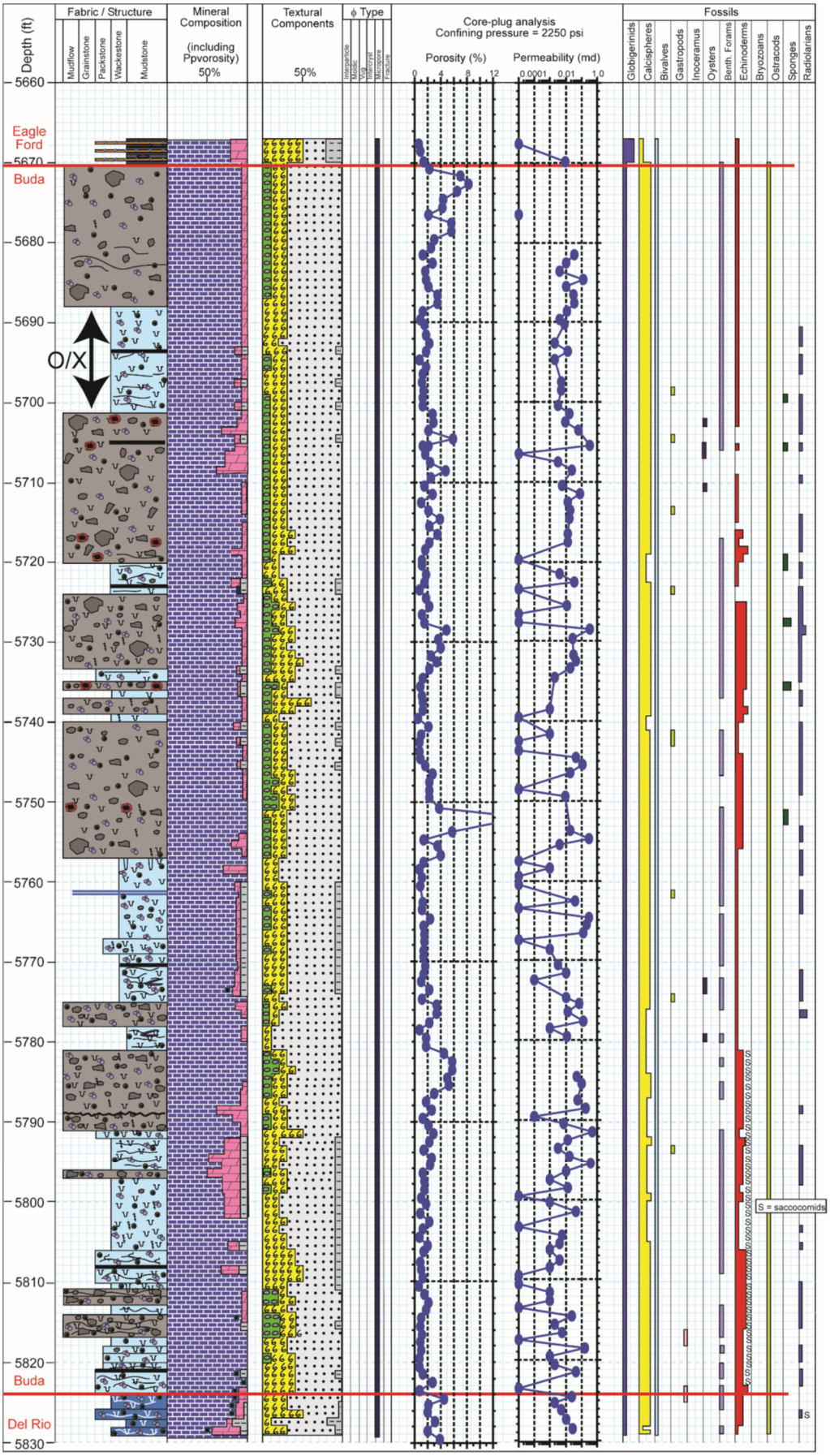

Figure 5. US Enercorp 1305H McKnight core description. Porosity and permeability values are from routine core-plug analysis. O/X = Oxidization/reduction alteration rims. API number = 421273633300. Core symbol legend shown in Figure 4.

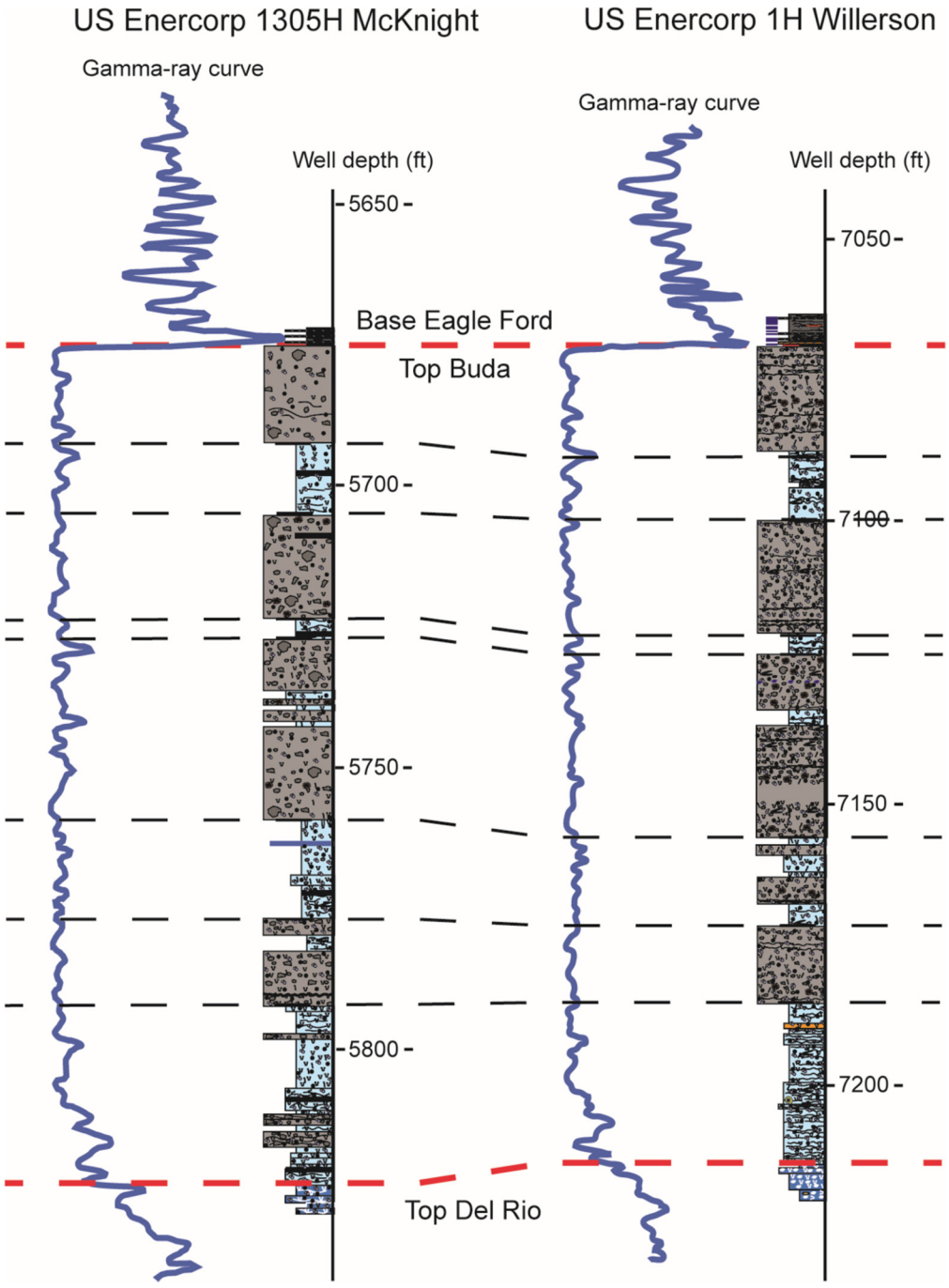

Figure 6. Correlation of the 1H Willerson and 1305H McKnight cores. Core descriptions are plotted along with gamma-ray curves. Correlation lines between cores are suggested time lines.

rare ammonites, and lesser benthic-derived sediments, including bivalves, gastropods, echinoid fragments, inoceramid fragments, oyster fragments, and benthic foraminifers. These sediments were highly bioturbated, with deep *Thalassinoides* burrows being common. The abundance of these burrows indicates well-oxygenated sediments, as do the other bottom dwellers.

Sedimentation is considered to have been below storm-wave base, as no oscillatory hydrodynamic features are present. If hydrodynamic features did form, they were later destroyed by bioturbation. Well-burrowed firmgrounds indicate that there were periodic hiatuses where sedimentation stopped or was very slow (Fig. 8B). Figure 13 shows the stages of formation of a firmground and the storm-return deposit above. Firmgrounds form when sedimentation slows down or ceases (Savrda et al., 2001). Mud shrimp or similar animals burrow deep into the muddy sediment where oxygenated (Fig. 13A). After a large storm (hurricane level?), the return flow created by the storm surge can carry muddy sediments (terrigenous-rich mud with intraclasts) seaward out onto the shelf as hyperpycnal density flows (e.g., Stow et al., 1998). These storm-return currents deposit muddy sediment, skeletal debris, and intraclasts within the large open *Thalassinoides* burrows and leave a layer of terrigenous-rich sediments above the firmground surface (Fig. 13B). The argillaceous layers commonly show *Planolites* burrows that may have taken advantage of freshly deposited organic matter. After the deposition of the argillaceous-rich sediments, normal carbonate mud-dominated sedimentation is reestablished. Upon later burial, compaction collapses the large burrows, and mechanical and chemical (solution seams) compaction produced the argillaceous seams (Fig. 13C). Scattered diagenetic fine-crystalline dolomite rhombs are common in the argillaceous seams.

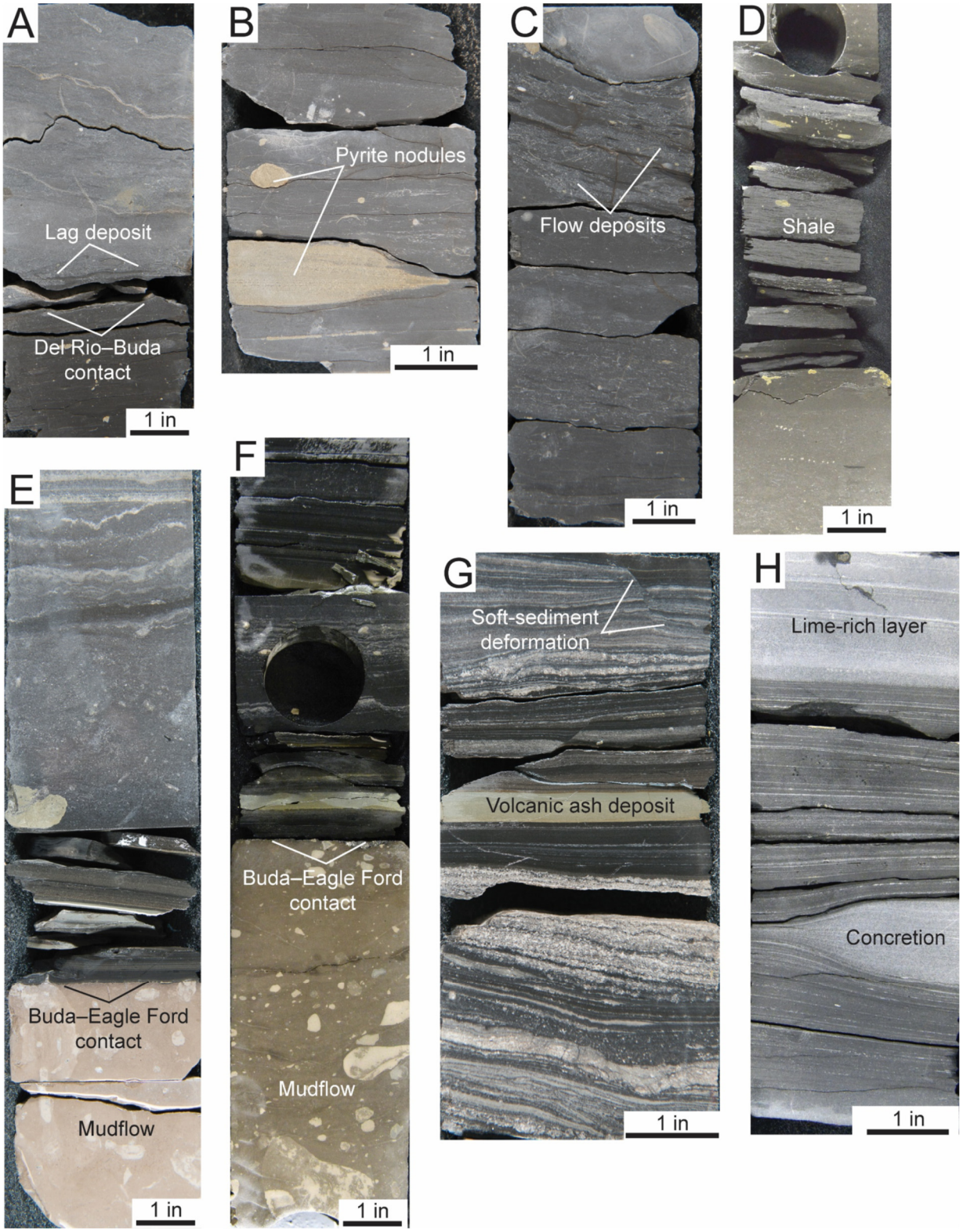

Figure 7. Lithofacies of Del Rio Formation and Eagle Ford Group. (A) Contact between the Del Rio and Buda formations. A lag deposit is at the base of the Buda section. The Del Rio section is more argillaceous. 1H Willerson, 7211.5 ft (2198.1 m). (B) Argillaceous lime wackestone with pyrite nodules in the Del Rio Formation. 1H Willerson, 7216 ft (2199.4 m). (C) Argillaceous lime wackestone with grainy flow layers in the Del Rio Formation. 1H Willerson, 7213 ft (2198.5 m). (D) Thin shale layer within lime wackestone in the Del Rio Formation. 1305H McKnight, 5826.7 ft (1776.0 m). (E) Contact between the Buda Limestone and Eagle Ford Group. The Buda section is a lime wackestone mudflow with soft-sediment clasts. The lower part of the Eagle Ford section is laminated, whereas the upper part is a massive gravity flow. 1H Willerson, 7059.7 ft (2151.8 m). (F) Contact between the Buda Formation and Eagle Ford Group. The Buda section is a lime wackestone mudflow with soft-sediment clasts. The Eagle Ford part is a very dark, organic-rich laminated mudstone. 1305H McKnight, 5669.6 ft (1728.1 m). (G) Laminated Eagle Ford calcareous mudstone with thin volcanic ash deposits showing soft-sediment deformation. 1H Willerson, 7058.6 ft (2151.5 m). (H) Laminated Eagle Ford mudstone with calcite concretion. 1305H McKnight, 5667.6 ft (1727.5 m).

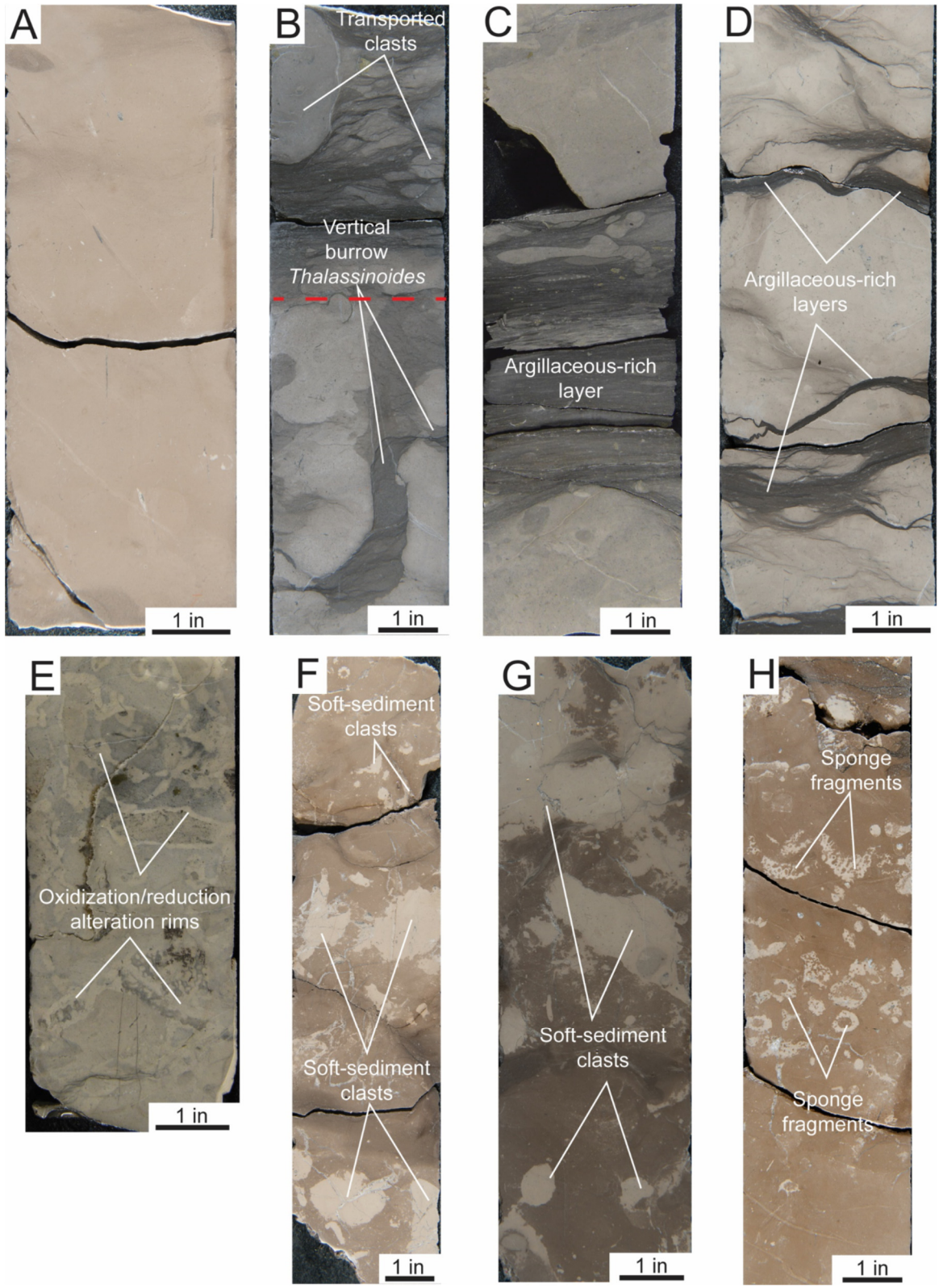

Figure 8. Buda Limestone lithofacies in core slabs. (A) Homogenous lime wackestone. 1H Willerson, 7108.5 ft (2166.7 m). (B) Well-burrowed lime wackestone with vertical *Thalassinoides* burrow. Red-dashed line marks top of burrowed firmground. Above firmground is a very argillaceous flow deposit that contains transported clasts. Burrows are filled with similar argillaceous sediment. 1H Willerson, 7200 ft (2194.6 m). (C) Interbedded lime wackestone and argillaceous-rich mudstone. Mudstone deposited by gravity-flow processes. 1305H McKnight, 5820.5 ft (1774.1 m). (D) Lime wackestone with compacted argillaceous mudstone seams. 1H Willerson, 7154.5 ft (2180.7 m). (E) Lime wackestone showing oxidization/reduction alteration rims. Section suggests long-term development of a firmground. 1305H McKnight, 5688.5 ft (1733.9 m). (F) Mudflow containing distorted soft-sediment rip-up lime mudstone clasts. 1H Willerson, 7179 ft (2188.2 m). (G) Mudflow containing distorted soft-sediment rip-up lime mudstone clasts. 1H Willerson, 7133.6 ft (2174.3 m). (H) Mudflow with transported sponge fragments. 1H Willerson, 7122 ft (2170.8 m).

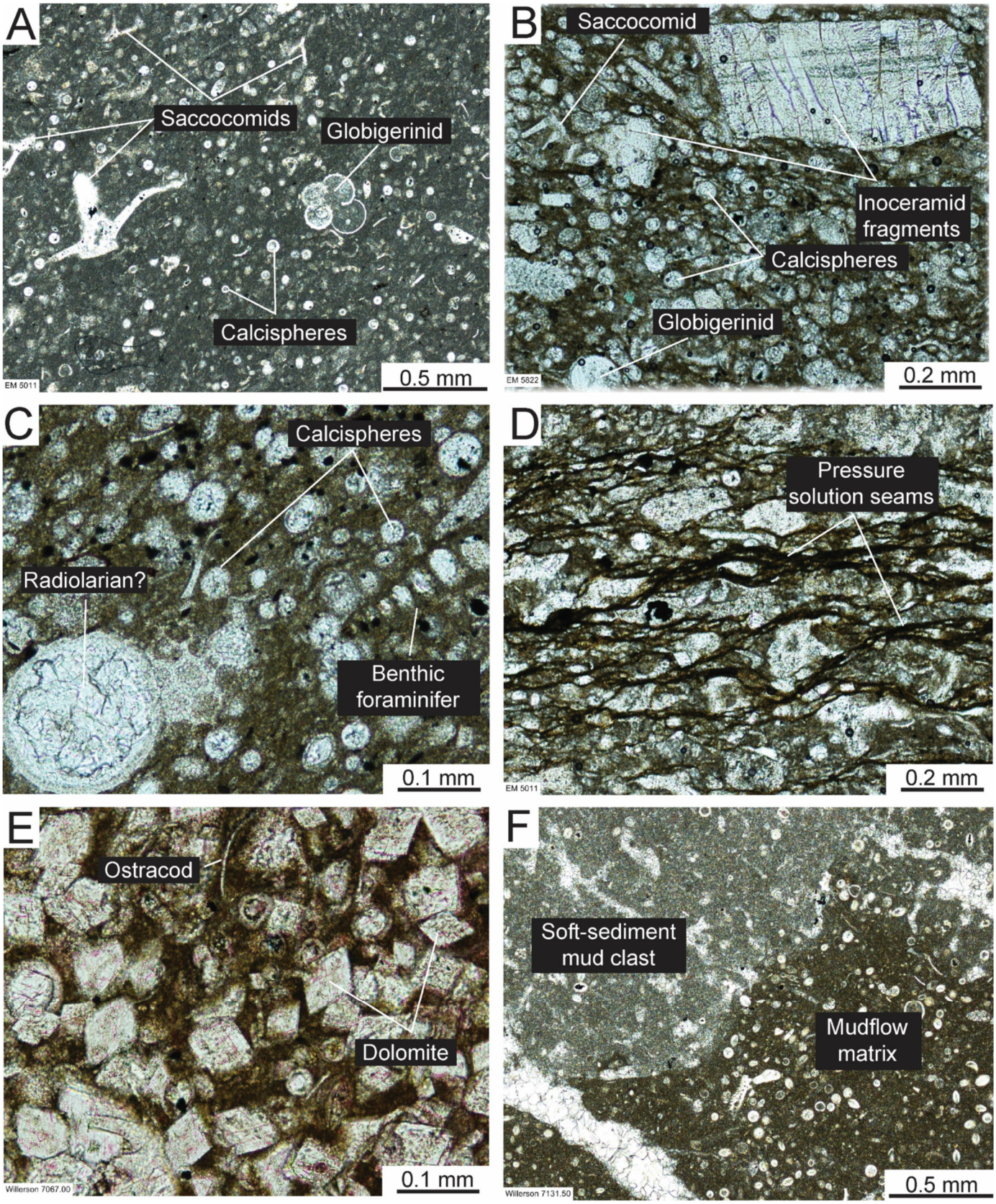

Figure 9. Buda Limestone lithofacies in thin section. (A) Peloidal lime wackestone with saccocomid fragment, globigerinid, and calcispheres. 1305H McKnight, 5011 ft (1527.4 m). (B) Peloidal lime packstone with inoceramid fragments, and calcispheres. 1305H McKnight, 5822 ft (1774.6 m). (C) Peloidal lime packstone with inoceramid calcispheres, benthic foraminifer, and possible radiolarian. 1305H McKnight, 5824 ft (1775.2 m). (D) Very argillaceous peloidal lime packstone with abundant solution seams. 1305H McKnight, 5811ft (1771.2 m). (E) Dolomite crystals in argillaceous solution seam. 1H Willerson, 7067 ft (2154.0 m). (F) Soft-sediment mud clast in lime wackestone matrix. Sample is from a mudflow. 1H Willerson, 7131.5 ft (2173.7 m).

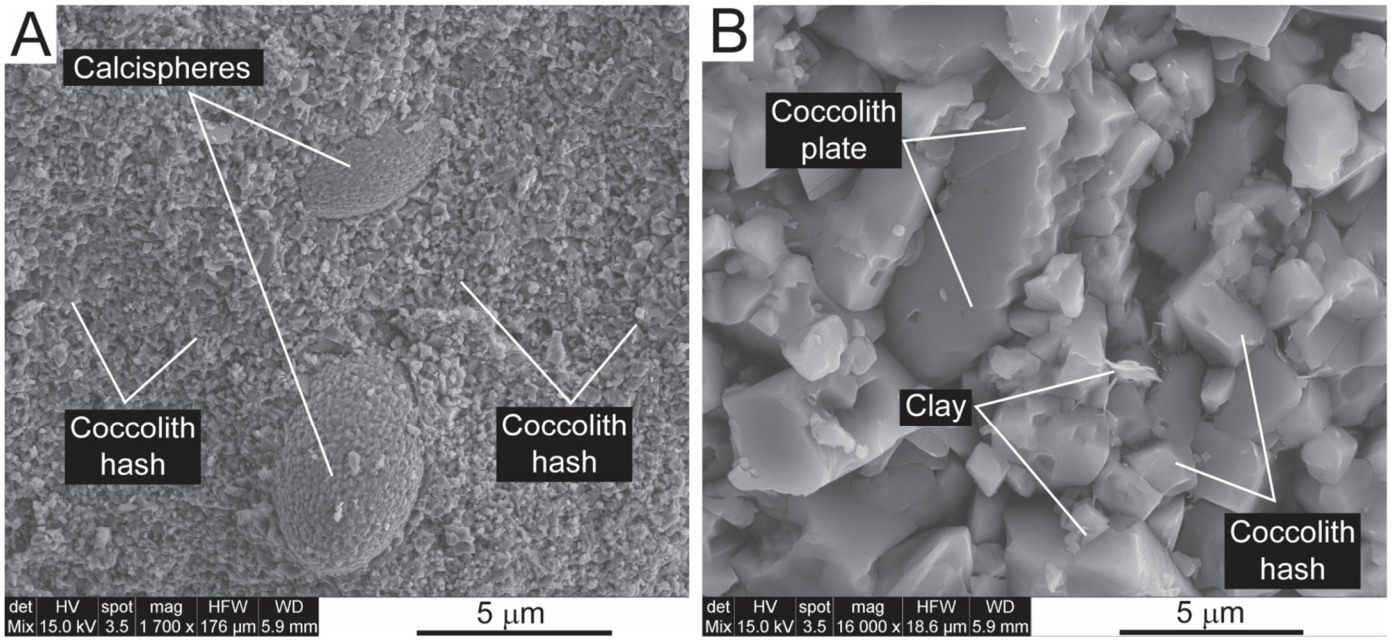

Figure 10. Scanning electron microscope images of Buda matrix. 1H Willerson, 7136.5 ft (2173.8 m). (A) Several calcispheres in a coccolith-hash matrix. (B) Close-up of a coccolith enclosed in coccolith hash. A few clay flakes are present.

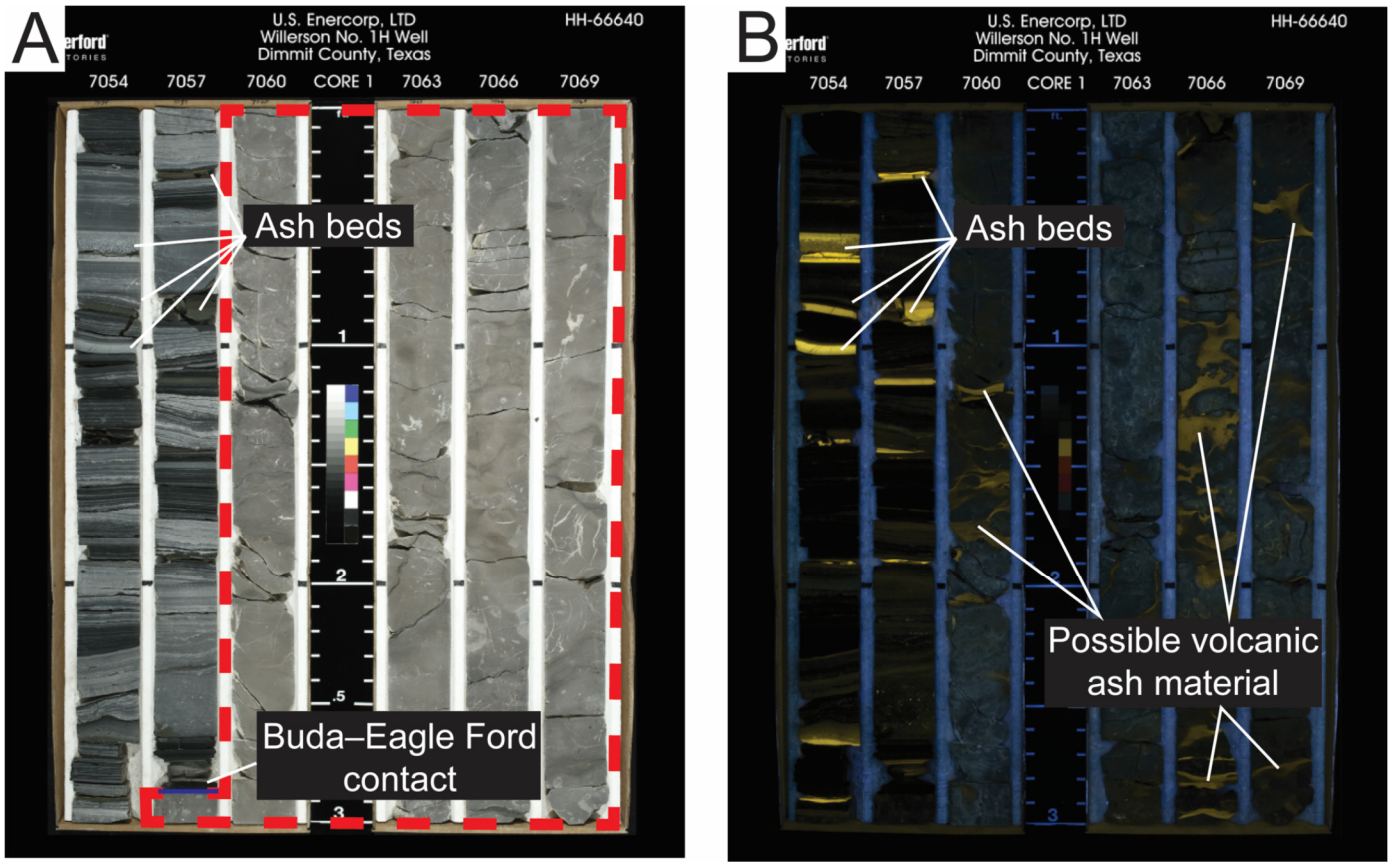

Figure 11. Buda and Eagle Ford volcanic ash. (A) Core interval covering contact between Buda and Eagle Ford sections. The Buda interval is composed of a mudflow (outlined by red-dashed box). Within the Eagle Ford section are well-preserved volcanic ash beds. 1H Willerson, 7054 ft (2150 m)–7072 ft (2156 m). (B) Same cored interval as A, but photographed with ultraviolet light. Eagle Ford volcanic ash layers strongly fluoresce. The fluorescence in the Buda is possibly related to volcanic ash material in argillaceous layers and burrows.

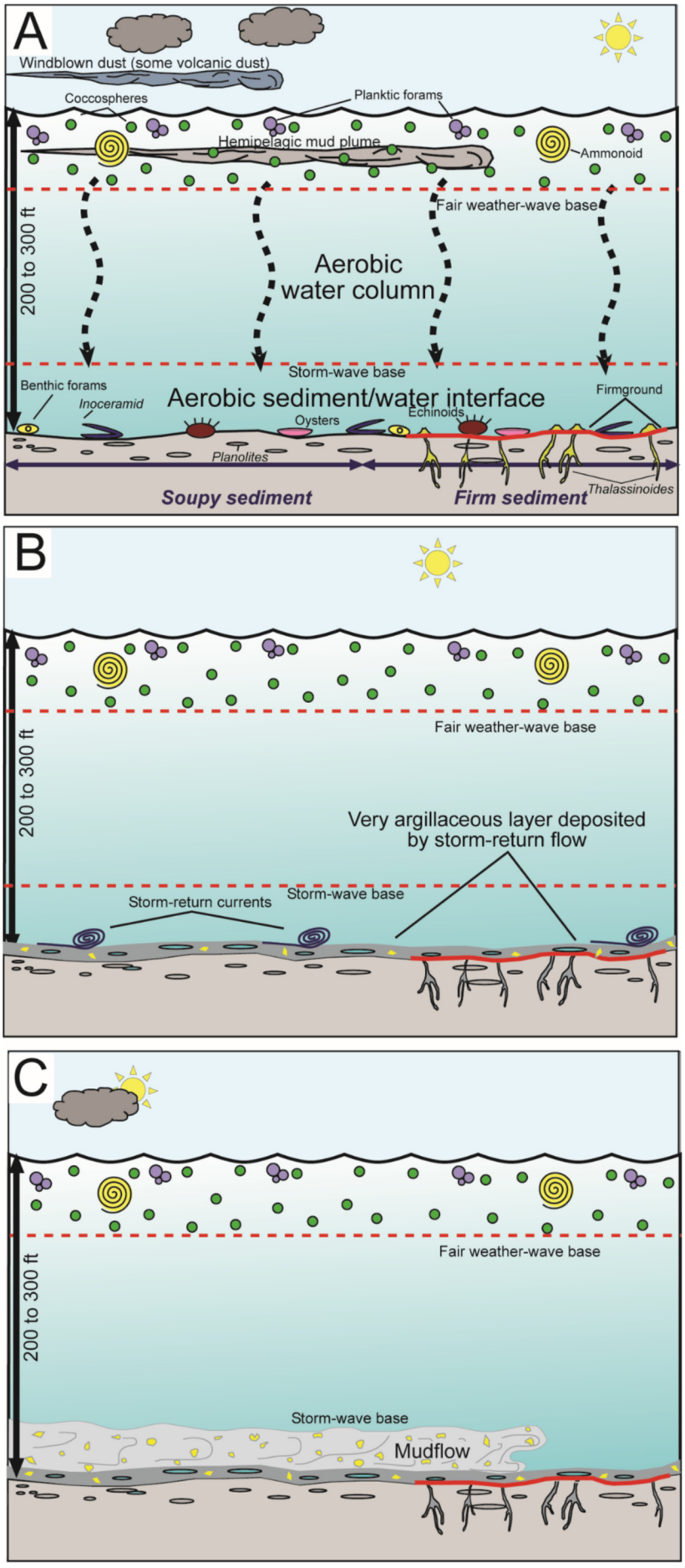

Figure 12. Buda Limestone depositional models. (A) General model for in-place deposition. Low-energy, slow deposition mainly by suspension. (B) Model for storm-return-flow deposition. Following major storms, updip sediment can be transported by downdip storm-return currents. (C) Model for mudflow deposition. Large, widespread mudflows transports mud and soft-sediment rip-up clasts downdip.

Mudflow Sedimentation

Interbedded with the in-place deposited strata are disturbed deposits that have abundant soft-sediment intraclasts and displaced fauna such as sponges (Figs. 8F–8H). These units range from 1 to 21 ft (0.3 to 6.4 m) thick (Fig. 6) and are interpreted as mudflows (Fig. 12C) composed of resedimented updip deeper water Buda sediments. These mudflows appear to have been cohesive, and some internal structures remained intact. Both burrows and argillaceous layers are present but show signs of deformation (Fig. 8F). Figure 6 shows apparent correlations between the 1H Willerson and 1305H McKnight wells that are 16 mi (27.4 km) apart and basically along strike (Fig. 1) with each other. The vertical distribution of the mudflows appears to be similar between the two wells, suggesting that many of the mudflows in each well are correlative and occurred at the same time. Hance (2003) presented a compilation of data on mass flows and summarized that widespread mass flows can occur on very low angle slopes of less than 2°. At these low angles, mass flows can have runouts as far as 500 mi (800 km) and cover areas up to 15,500 mi^2 (40,000 km^2). Therefore, the suggestion that Buda mudflows could have been at least 16 mi (27.4 km) wide is very reasonable.

The mudflow units appear as dark gray, whereas the original in-place sediments are light gray. Porosity, permeability, and unconfined compressive strength measurements differ between the in-place and mudflow units. As seen in Table 1, porosity and permeability are lower in the in-place units. Mean porosity in the in-place units is 1.4%, as compared with the mean porosity of 3.2% in the mudflow units, and mean permeability in the in-place units is 0.001 md, as compared with the mean permeability of 0.019 md in the mudflow units. UCS shows a higher mean value for the in-place units (17,825 psi [122.9 MPa]), as compared with the mudflow units (15,925 psi [109.8 MPa]). These results showing UCS measurements inversely correlating with porosity correspond to what Zahm and Enderlin (2010) and Zahm and Kerans (2012) found in various carbonate rock types they investigated; that is, UCS and porosity are inversely correlated. The underlying mechanism that produces the physical change between in-place and mudflow sedimentation may be a modification of packing arrangement in the mudflow by the transport mechanism. This change in packing arrangement in chalks has been well documented by Brasher and Vagle, (1996), van der Molen (2004), and Fabricius (2007) for chalks in the North Sea.

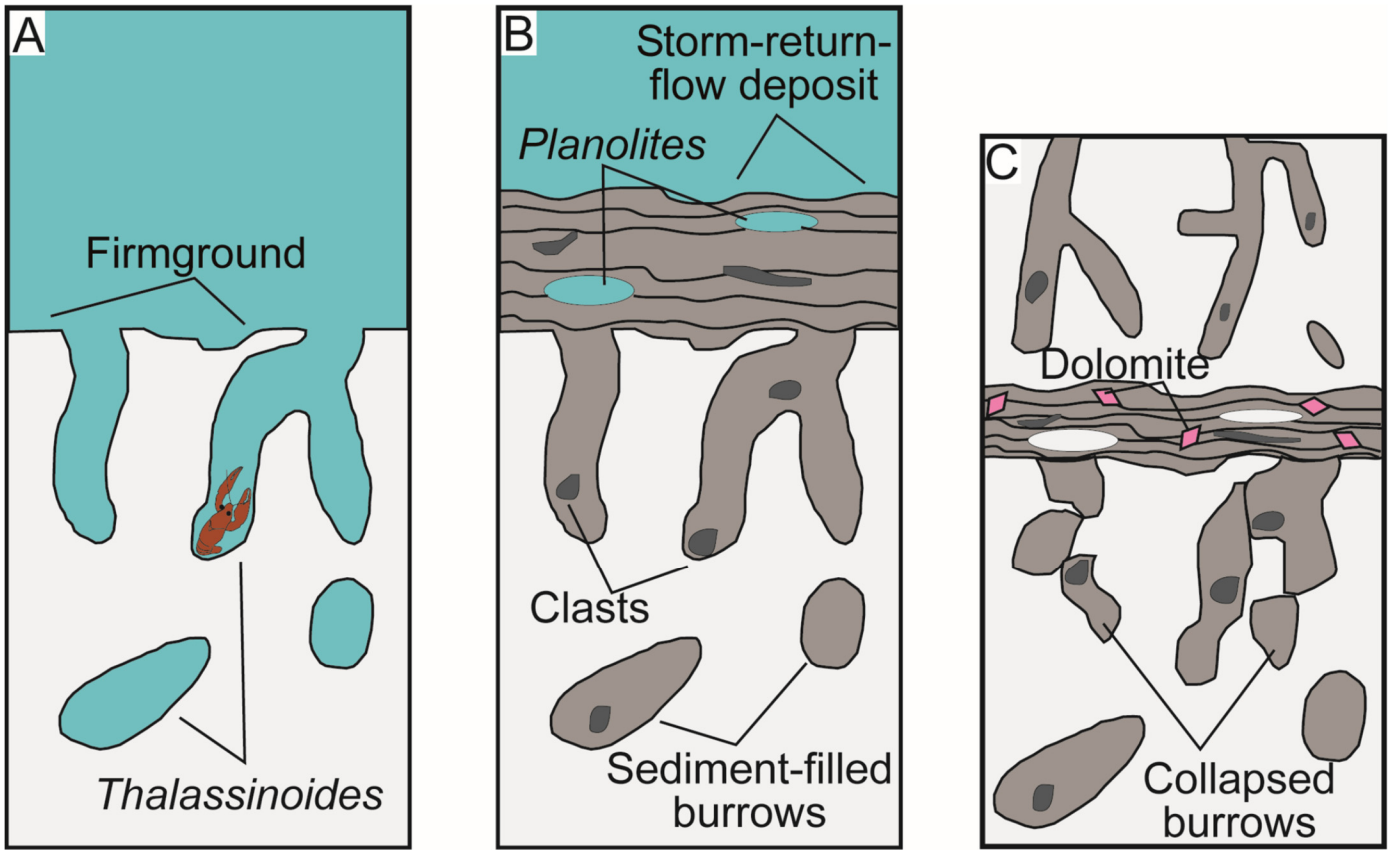

Figure 13. Model for firmground and storm-return deposits. (A) Burrowed firmground develops during a hiatus. (B) Hyperpycnal storm-return-flow deposits a very argillaceous-rich mud layer over the firmground surface and fills in the open burrows. The flow commonly contains soft-sediment clasts and other skeletal allochems; however, all the flow sediments appear to be composed of redeposited deeper water material. (C) After the flow subsides, normal chalk sedimentation resumes and is again bioturbated. Upon burial into the subsurface, extensive compaction occurs in the very argillaceous sediments, and dolomite forms. Some large vertical burrows compact and deform.

PORE NETWORKS

The Buda Limestone is a well-established fractured reservoir (e.g., Snyder and Craft, 1977), but some late hydrocarbon production may be contributed from the tight matrix, as seen in unconventional reservoirs. In this section the pore networks displayed by the cores are discussed. The pores are divided between fractures and matrix pores.

Fracture Pores

The Buda Limestone is known to produce hydrocarbon (e.g., Snyder and Craft, 1977) from fractures associated with tectonic elements, such as arches, flexures, and faults, and these fractures commonly have high angles of dip, which are less likely to be intersected in vertical cores. A borehole image log was collected within the McKnight well, and several partially open fractures were interpreted (Zahm et al., 2019, this volume). However, examination of cores and image logs suggests that faults were not encountered in these two wells. The fractures that are present are mainly occluded with calcite, and because of coring disturbance some thin-fracture pore openings cannot be stated with confidence as natural openings. None of the fractures appear to be long, through-going fractures, and most terminate at argillaceous seams and/or stylolites. The fractures appear to be related to compacted intervals between solution seams and stylolite tension fractures (Fig. 14). Details of the fracture analysis from these two cores and image log analyses can be found in Zahm et al. (2019, this volume).

Matrix Pores

Through analysis of Ar–ion-milled samples on the scanning electron microscope (SEM), the pores observed in the Buda matrix range in size from ~10 nm up to 1 µm (Fig. 15). The associated mean pore-throat radius ranges from 5 to 200 nm as calculated from MICP analysis (Figs. 16C and 16D).

Blue-fluorescent-dye-impregnated thin sections display the nanopores to micropores as a faint blue haze (Fig. 17). The pores are much too small to be resolved individually in thin section. The nanopores to micropores may occur as patches in the thin section, or transported mud clasts may exhibit nanopores to micropores, whereas the adjacent matrix does not (Fig. 17B). SEM analysis is necessary to distinguish and characterized the nanopores to micropores.

SEM image analysis shows that the nanopores to micropores are associated with microrhombic calcite (Fig. 15). The nanopores and micropores result from the incomplete cementation of the original void space between coccolith plates and coccolith elements. The calcite microrhombs range between 0.5 and 4 µm, are euhedral in shape, and show growth interference and resulting interlocking of crystals (Figs. 15E and 15F). The nanopores have triangular to diamond shapes (e.g., Fig. 15E) characteristic of pores surrounded by crystal faces. Within some of the pores are

Table 1. Core-plug porosity and permeability data and unconfined compressive strength measurements for in-place and mud-flow sedimentation.

Depositional Class	In-place sedimentation	Mud-flow sedimentation
Unconfined compressive strength	17,825 psi (122.9 MPa)	15,925 psi (109.8 MPa)
Core-plug porosity	1.4%	3.2%
Core-plug permeability	0.001 md	0.019 md

submicrometer clay platelets (e.g., Fig. 15F). These clay platelets reduce connectivity of the pores and, thus, permeability.

RESERVOIR QUALITY

Core-Plug Evaluation of Matrix Reservoir Quality

Matrix reservoir quality of the Buda section in the area of investigation is very low according to conventional core-plug analysis. Most porosity values are less than 5%, and most permeability values are less than 0.1 md (Fig. 18). Snyder and Craft (1977) noted the same level of reservoir quality for the Buda matrix in South Texas. They also added that measured permeability in whole core samples that contain fractures was in excess of 2000 md. Permeability values shown in Figure 18 that are higher than 0.01 md and associated with low porosity values (less than 3%) are suggested to be related to fractured plugs. The two studied cores provide different populations of porosity and permeability values (Fig. 18). The two cores have a similar porosity range (~1 to 5%) but a different permeability range. The 1305H McKnight permeability values are higher than the 1H Willerson values, and many of the 1305H McKnight permeability values are in the probable fractured-plug zone (Fig. 18). Also, permeability values equal to or less than 0.0001 md appear to be too low to measure. The difference in measured permeability values may be related to two different vendors performing the measurements. Also, POROLABS analyzed the 1305H McKnight samples at 800 psi (5.52 MPa), whereas Weatherford Laboratories analyzed the 1H Willerson sample at 2250 psi (15.51 MPa). Analyzing porosity and permeability at different confining pressures may be the reason that the 1H Willerson permeabilities are lower, as those samples were run at higher confining pressures.

The 1H Willerson core shows zones of dark and light shaded limestone. The darker zones are interpreted as mudflows on the basis of the presence of soft-mud clasts (Figs. 3 and 5). The lighter zones are interpreted as the in-place mud matrix. This is an important observation as the mudflow zones generally have higher porosities and permeabilities than the in-place matrix zones, as noted earlier (Table 1).

MICP Evaluation of Matrix Reservoir Quality

MICP analysis provides insight into reservoir quality (Fig. 16). Calculated pore-throat mean radii are generally less than 0.2 µm (200 nm) with several samples having pore-throat mean radii of ~0.005 µm (5 nm) (Figs. 16C and 16D). These very small pore-throat sizes are very restrictive to two-phase flow, especially oil flow.

The MICP injection curves (Figs. 16A and 16B) show very high initial injection pressures generally ranging between 800 (5.52 MPa) and 7000 psi (48.3 MPa). High injection pressures are associated with small pore-throat radii. Each injection curve was color coded according to permeability classes (Figs. 16A and 16B). However, because of the difficulty of accurately measuring permeability values less than ~0.001 md, some of the classified injection curves may not have a valid permeability measurement. Even with this restriction, the higher permeability samples do correlate with the lower injection pressures, and the lower permeability samples do correlate with the higher injection pressures.

Hydrocarbon Production

An interesting speculation about the hydrocarbon production from the two wells investigated is how much production is from fracture pores and whether some production, if any, comes from the matrix pores. We suggest that the early production is from the fractures and that later production after the fractures are drained and pressure is lowered is in part from the matrix pores. Matrix porosity may contribute some oil into the large surface void area created by fractures, but not enough to significantly contribute to enhanced production that keeps the decline curve from rapidly decreasing. The decline curve from the 1 Willerson well supports this assumption (Fig. 19). The well production history shows a sharp decline curve for both oil land gas.

CONCLUSIONS

The Buda Limestone was deposited on the drowned Lower Cretaceous South Texas shelf during the transgressive leg of the Cenomanian 101–96 Ma composite sequence. As reflected by the original sediment mixture of planktic biotas, especially coccolith hash, calcispheres, and planktic foraminifers, and lesser benthic biotas and abundance of deep-sediment bioturbation, Buda sedimentation is interpreted to have occurred in a below-storm-wave-base, aerobic, quiet-water depositional setting on the outer shelf. Two major depositional facies are recognized: (1) in-place sedimentation (lime wackestones and packstones with very argillaceous seams) of argillaceous coccolith-fragment-rich mud containing mainly planktic foraminifers and calcispheres with rare benthic fauna, and (2) mudflows of resedimented-in-place sediment, some of which was eroded and deposited as soft-sediment clasts. The mudflows between the 1305H McKnight and the 1H Willerson wells appear to correlate, suggesting that the mudflows were widespread (at least 16 mi [27.4 km] laterally).

The major hydrocarbon production from the Buda Limestone is from fracture pores. The matrix has low reservoir quality with nanopores to micropores. Porosity ranges from less than 1 to 5%, and permeability is generally less than 0.1 md. Pore throats are all in the micropore range (5 to 200 nm radii).

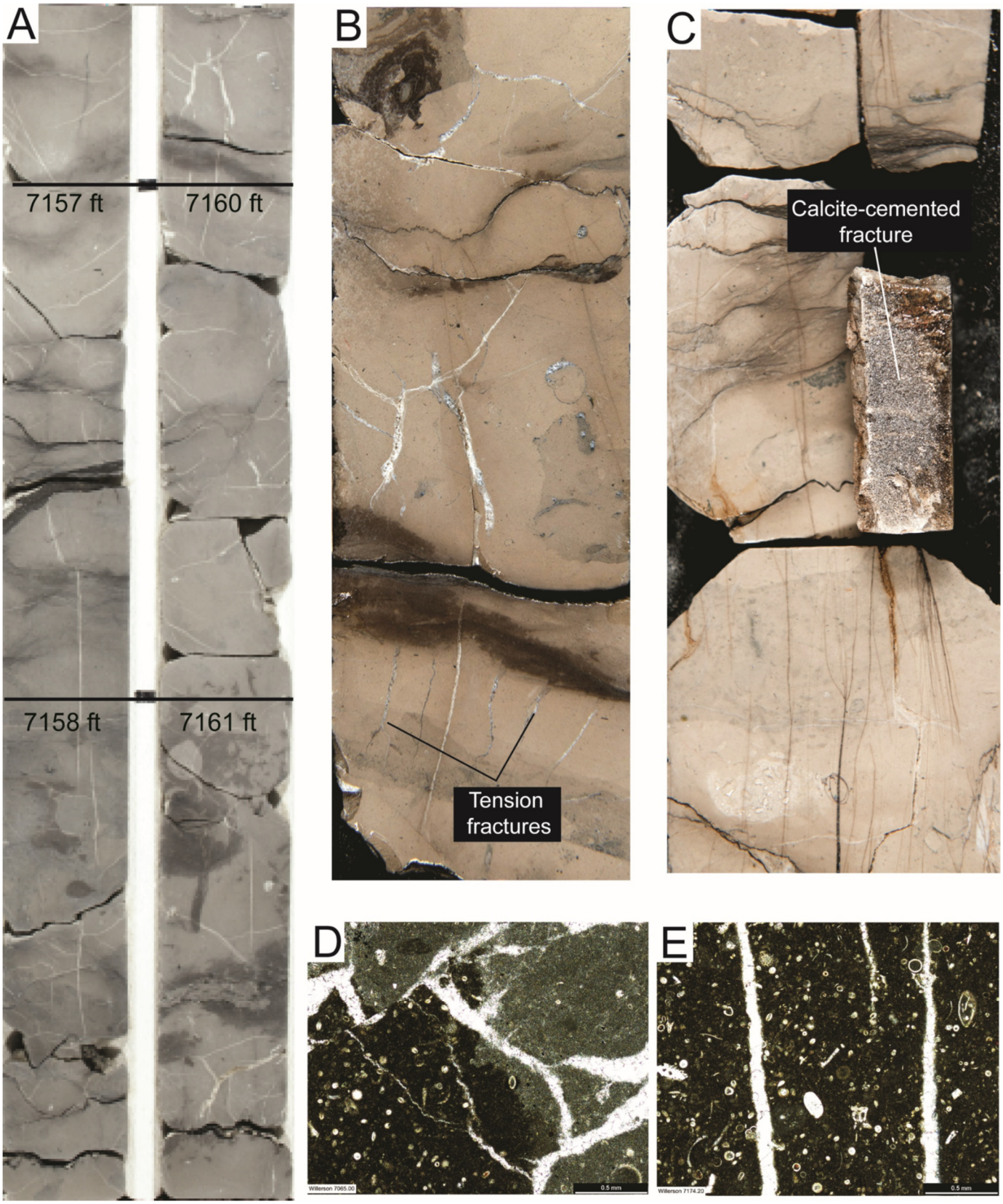

Figure 14. Buda Limestone fractures. (A) Several feet of core from the 1305H McKnight well showing multiple calcite-filled fractures. Some of the fractures are near vertical and terminate at argillaceous-rich solution seams. Other fractures are randomly orientated. 1305H McKnight, 7157–7162 ft (2181.5–2183.0 m). (B) Several styles of fractures are present. Those fractures that are in the middle of the slab are considered compaction fractures resulting from compaction of adjacent pressure solution seams. Associated with the stylolites are tension fractures. 1305H McKnight, 7159.6 ft (2182.2 m). (C) Numerous long and thin vertical fractures, many of which terminate at pressure solution seams. Fractures appear to be filled with hydrocarbon. 1H Willerson, 7191.5 ft (2192.0 m). (D) Random-orientated calcite-filled fractures in thin section. 1H Willerson, 7065.0 ft (2153.4 m). (E) Vertical calcite-filled fractures in thin section. 1H Willerson, 7174.2 ft (2186.7 m).

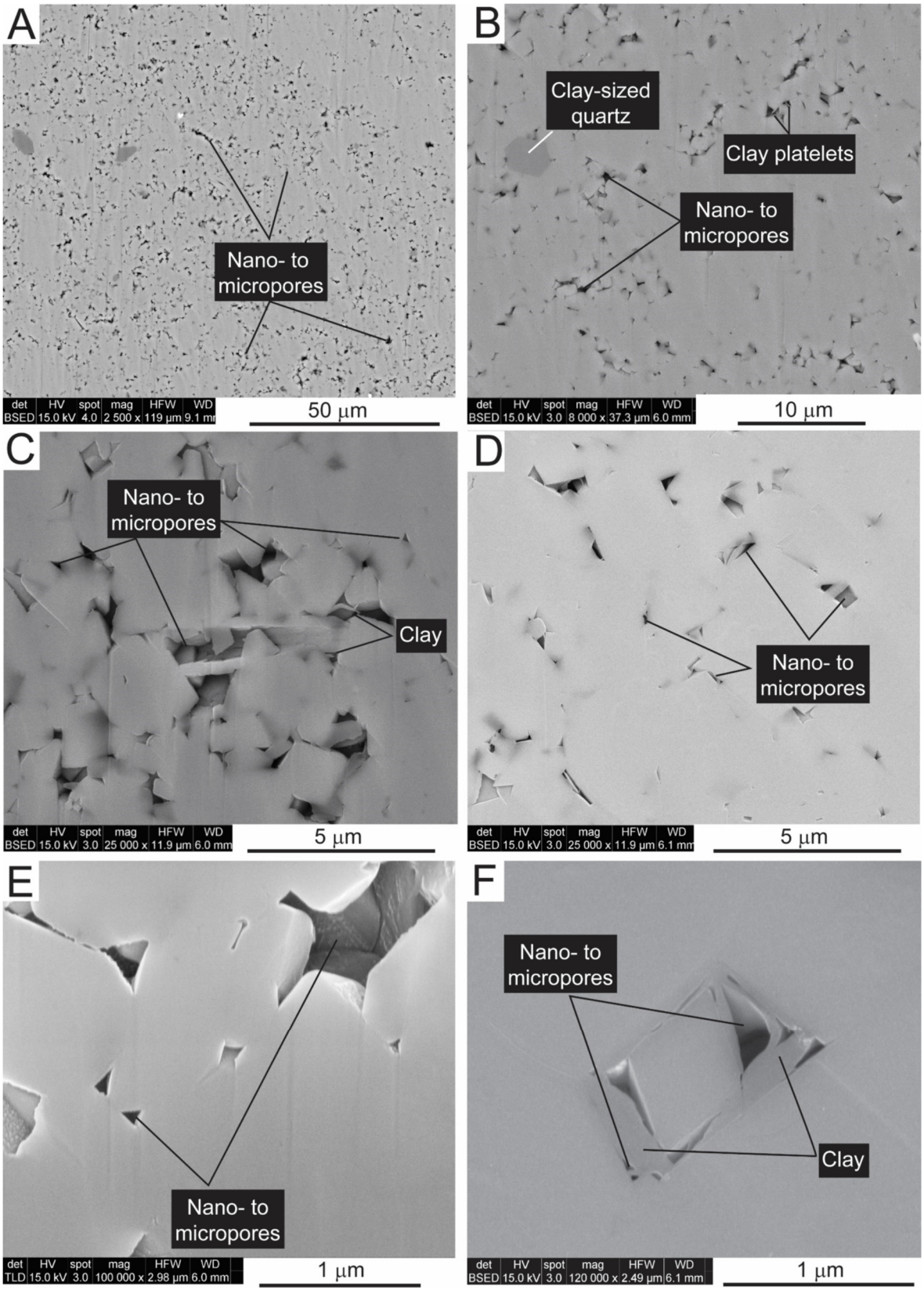

Figure 15. Scanning electron microscope images from Ar–ion-milled samples showing nanopores and micropores. (A) General view of nanopores and micropores in coccolith hash. Darker grains are quartz and albite silt. 1H Willerson, 7175.6 ft (2187.4 ft). (B) Close-up view of A showing nanopores and micropores between micrometer-scale calcite crystals (overgrowths on coccolith elements). 1H Willerson, 7175.6 ft (2187.4 m). (C) Nanopores and micropores with some clay platelets. 1H Willerson, 7175.6 ft (2187.4 m). (D) Interparticle nanopores and micropores between coccolith fragments. Coccolith fragments are well cemented. 1H Willerson, 7181.6 ft (2199.0 m). (E) Close-up of nanopores and micropores. Cementation is locking the microcrystals together. 1H Willerson, 7175.6 ft (2187.4 m). (F) Micropore divided into nanopores by a calcite nanocrystal and clay platelets. 1H Willerson, 7091.5 ft (2161.5 m).

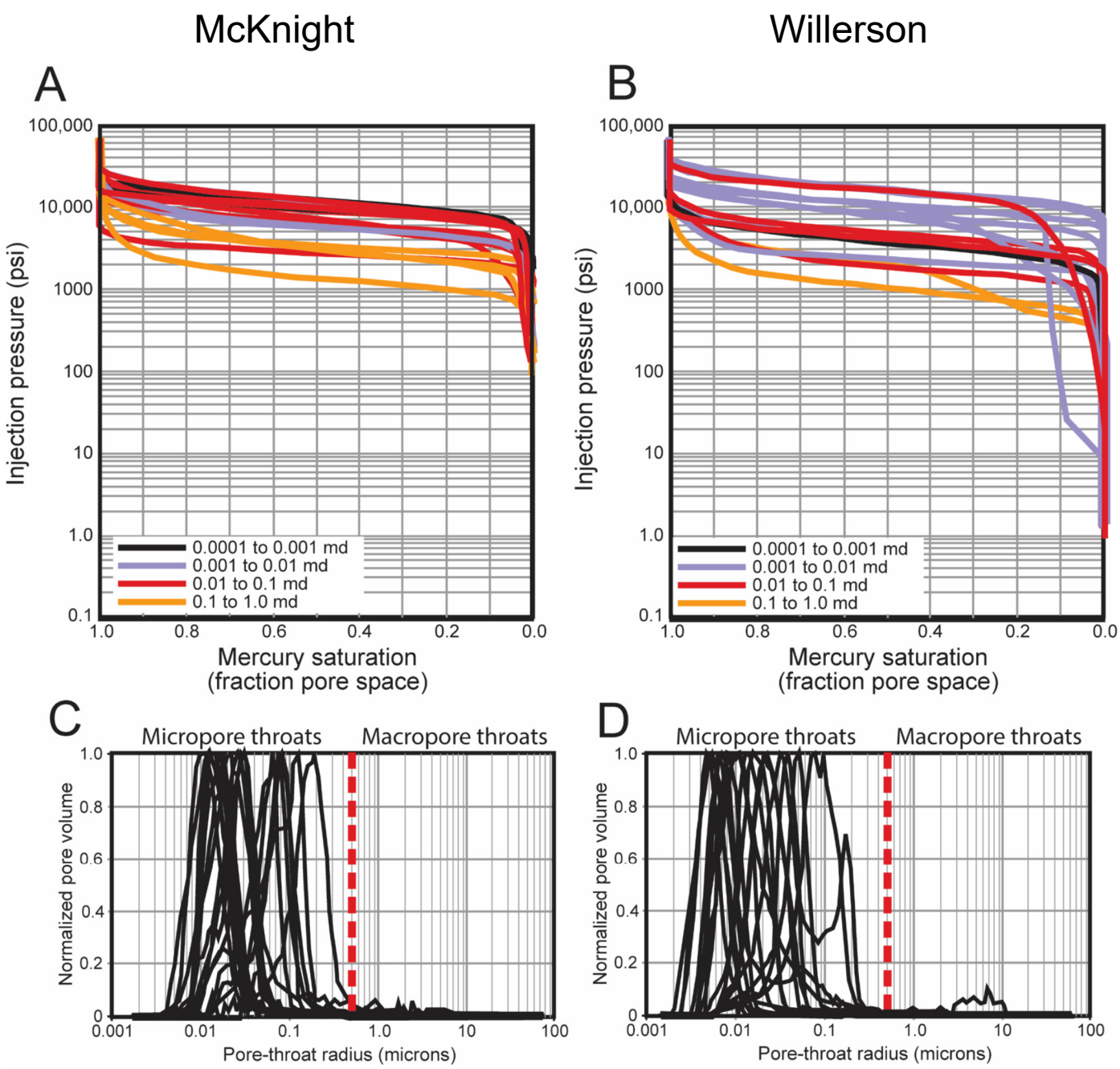

Figure 16. Mercury injection capillary pressure (MICP) analysis data. (A) 1305H McKnight core MICP injection pressure curves separated by permeability classes. (B) 1H Willerson core MICP injection pressure curves separated by permeability classes. (C) Normalized pore volume versus pore-size distribution plots from MICP data for the 1305H McKnight core. (D) Normalized pore volume versus pore-size distribution plots from MICP data for the 1H Willerson core.

Initial production is related to the fracture pore network, but later production may have contribution from the matrix pore network.

This investigation provides a sound geologic characterization of the Buda Limestone in South Texas. The study provides new insights into depositional processes and matrix pore networks. Description of additional cores is important to assess the present conclusions and to determine additional geologic characterization concepts.

ACKNOWLEDGMENTS

We want to recognize the Carbonate Reservoir Characterization Research Laboratory (RCRL) at the Bureau of Economic Geology and associated sponsors for support of this investigation. Production data were provided by IHS Markit Energy (Englewood, Colorado). Patrick Smith of the Bureau helped with the SEM images. We appreciate the reviews of the manuscript by Ahmed Alnahwi, Brian Lock, and Kim Patty. Susie Donges of the Bureau of Economic Geology edited the manuscript, and we thank her for her effort. Publication authorized by the Director, Bureau of Economic Geology, Jackson School of Geosciences, University of Texas at Austin.

REFERENCES CITED

Ak, O., 2015, The depositional environment and the diagenetic processes of the Buda limestone (Cenomanian) in south-

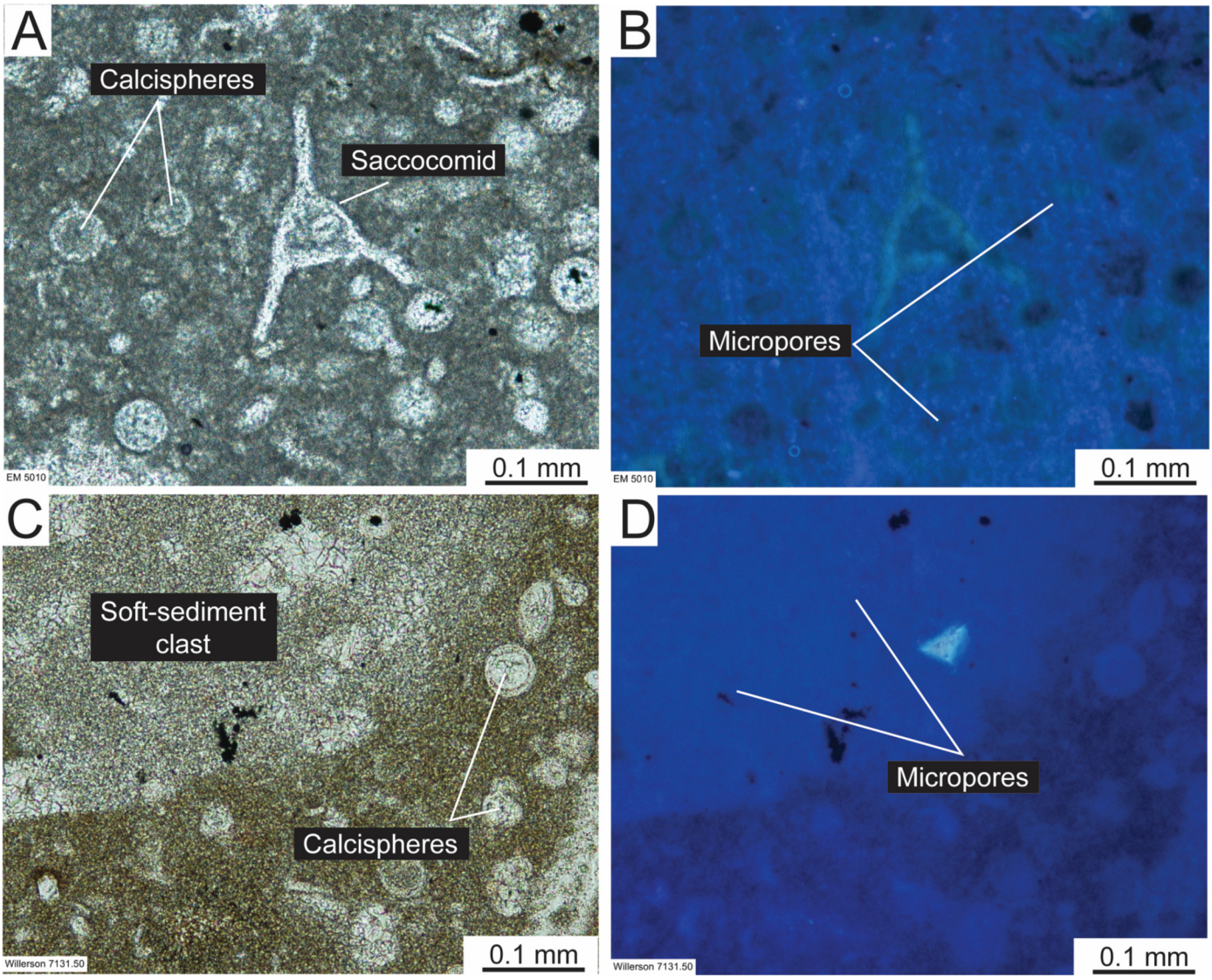

Figure 17. Microporous thin sections. (A) Lime wackestone with calcispheres and saccocomid fragment. 1305H McKnight, 5010 ft (1527.0 m). (B) Same as A, but taken under ultraviolet (UV) light. Micropores show up as a blue fluorescent haze. (C) Lime wackestone with calcispheres and soft-sediment clast. 1H Willerson, 7131.5 ft (2173.7 m). (D) Same as C, but taken under UV light. Micropores show up as a blue fluorescent haze.

central Texas: M.S. Thesis, University of Texas at San Antonio, 81 p.

Alnahwi, A., R. G. Loucks, S. C. Ruppel, R. W. Scott, and N. Tribovillard, 2018, Dip-related changes in stratigraphic architecture and associated sedimentological and geochemical variability in the Upper Cretaceous Eagle Ford Group in South Texas: American Association of Petroleum Geologists Bulletin, v. 101, p. 2537–2568, <https://doi.org/10.1306/05111817310>.

Blakey, R. C., 2016, Paleogeography and geologic evolution of North America: Images that track the ancient landscapes of North America (Late Cretaceous–75 Ma): Northern Arizona University Geology Department, Flagstaff, Arizona <http://jan.ucc.nau.edu/rcb7/nam.html>.

Brasher, J. E., and K. R. Vagle, 1996. Influence of lithofacies and diagenesis on Norwegian North Sea chalk reservoirs: American Association of Petroleum Geologists Bulletin, v. 80, p. 746–769.

Butler, R. W., 2009, Biostratigraphy of the Del Rio Formation of West Texas: M.S. Thesis, University of Louisiana at Lafayette, 41 p.

Darbonne, N., 2012, Buda beneath: Oil and Gas Investor, <https://www.hartenergy.com/exclusives/buda-beneath-12375>.

Davis, G., G. Wilcox, M. Amone, and S. Bruington, 2016, Rejuvenating the Buda Limestone reservoir in Texas by using crude oil and nitrogen injection in underbalanced regime: Case history: Society of Petroleum Engineers Paper SPE–179715–MS, Richardson, Texas, 23 p., <https://doi.org/10.2118/179715-MS>.

Dawson, W. C., 1986, Austin Chalk and Buda Limestone (Cretaceous) petroleum reservoirs in Caldwell County, Texas—A case history: Energy & Exploitation, v. 4, p. 377–386, <https://doi.org/10.1177/014459878600400503>.

Denne, R. A. J. A. Breyer, T. H. Kosanke, J. M. Spaw, A. D. Callender, R. E. Hinote, M. Kariminia, N. Tur, Z. Kita, J. A. Lees, and H. Rowe, 2016, Biostratigraphic and geochemical constraints on the stratigraphy and depositional environments of the Eagle Ford and Woodbine groups of Texas, *in* J. A. Breyer, ed., The Eagle Ford Shale—A renaissance in U.S. oil production: American Association of Association of Petroleum Geologists Memoir 110, Tulsa, Oklahoma, p. 1–86, <https://doi.org/ 10.1306/13541957M1103660>.

Donovan, A. D., T. S. Staerker, A. Pramudito, W. Li, M. J. Corbett, C. M. Lowery, A. M. Romero, and R. D. Gardner, 2012, The Eagle Ford outcrops of West Texas: A field laboratory for understanding heterogeneities within unconventional mud-

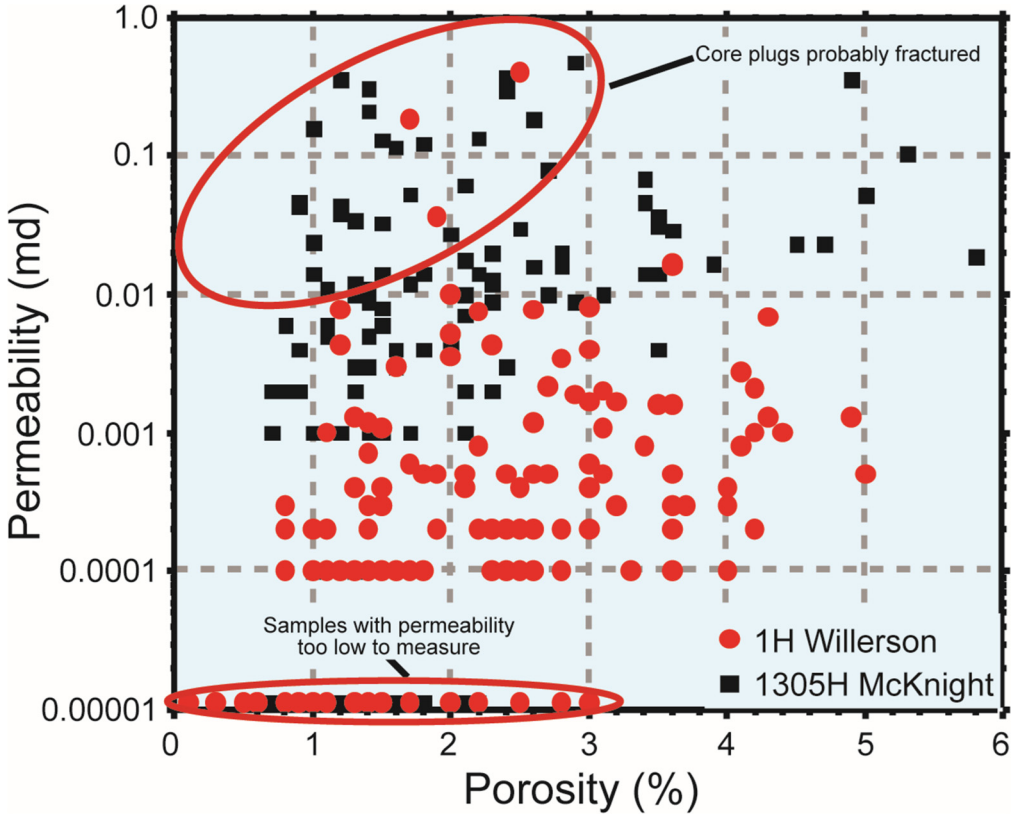

Figure 18. Core-plug porosity versus core-plug permeability. The data that line up along the 0.00001 md line are too low to measure and the data that line up along the 0.0001 and 0.0002 md lines are samples where permeability cannot be accurately measured with routine core plug analysis methods.

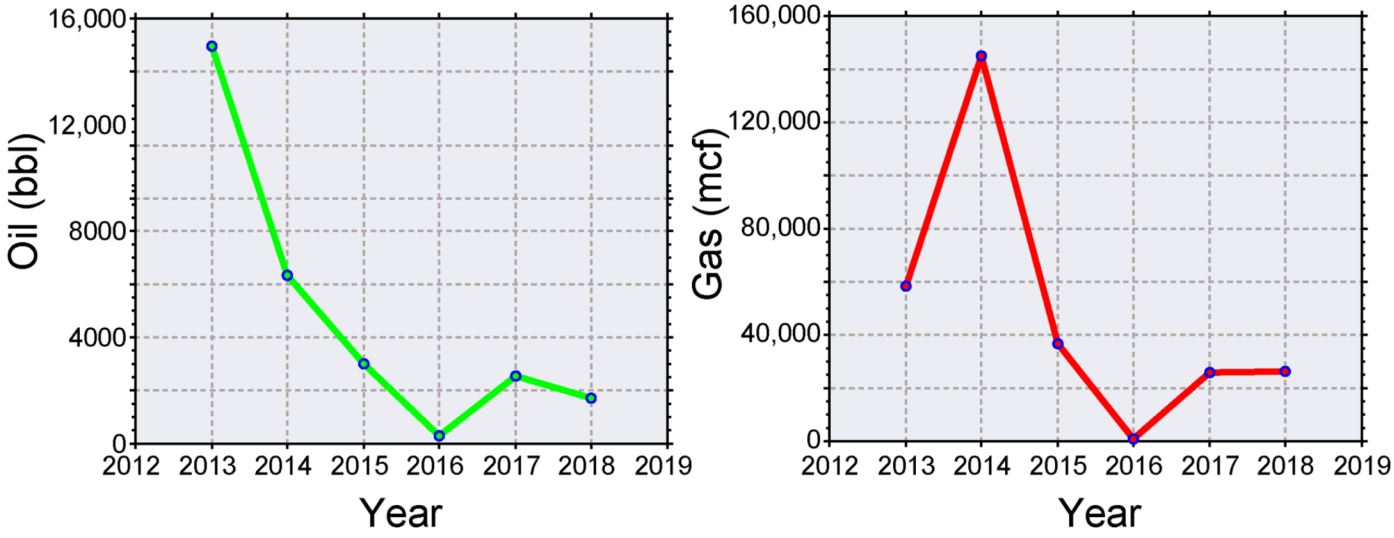

Figure 19. Oil and gas decline curves for the 1H Willerson well. Decline in oil and gas is fairly rapid. Graphs are based on data from IHS Markit Energy.

stone reservoirs: Gulf Coast Association of Geological Societies Journal, v. 1, p. 162–185, <https://www.gcags.org/Journal/2012.GCAGS.Journal/GCAGS.Journal.2012.vol1.p162-185.Donovan.et.al.pdf>.

Erdogan, S. L., 1969, Microbiofacies of the Cenomanian Buda Limestone (Comanche Cretaceous) of West and Trans-Pecos Texas: M.S. Thesis, Louisiana State University, Baton Rouge, 58 p.

Fabricius, I. L., 2007, Chalk: Composition, diagenesis and physical properties: Bulletin of the Geological Society of Denmark, Copenhagen, v. 55, December issue, p. 97–128.

Hance, J. J., 2003, Submarine slope stability: Project report prepared for the Minerals Management Service under the MMS/OTRC Cooperative Research Agreement 1435–01–99–CA–31003, Task Order 18207, MMS Project 421, Restin, Virginia, 245 p.

Hendrix, C. K., 2016, Chemolithofacies of the Upper Cretaceous Buda Formation and Austin Chalk Group, south-central Texas: A product of integration of lithologic and chemical data: M.S. Thesis, University of Texas at Austin, 127 p.

Hixon, R. T., 1959, Facies and petrography of the Cretaceous Buda Limestone of Texas and northern Mexico: M.S. Thesis, University of Texas at Austin, 152 p.

Lock, B. E., F. S. Bases, and R. A. Glaser, 2007, The Cenomanian sequence stratigraphy of Central to West Texas: Gulf Coast Association of Geological Societies Transactions, v. 57, p. 465–479.

Lock, B. E., R. W. Butler, and R. T. Franklund, 2009, Tempestite sedimentation: An example from the Del Rio Formation of West Texas: Gulf Coast Association of Geological Societies Transactions, v. 59, p. 463–476.

Loucks, R. G., 2018, Eagle Ford–A depositional setting and processes in southwestern Texas: An example of deeper-water, below-storm-wave-base carbonate sedimentation on a drowned shelf: Gulf Coast Association of Geological Societies Journal, v. 7, p. 59–78, <https://www.gcags.org/Journal/2018.GCAGS.Journal/2018.GCAGS.Journal.v7.04.p59-78.Loucks.pdf>.

Loucks, R. G., R. M. Reed, S. C. Ruppel, and D. M. Jarvie, 2009, Morphology, genesis, and distribution of nanometer-scale pores in siliceous mudstones of the Mississippian Barnett Shale: Journal of Sedimentary Research, v. 79, p. 848–861, <https://doi.org/10.2110/jsr.2009.092>.

Parker, R. M., 2000, The Lower Cretaceous Buda Limestone Formation in Gonzales County, Texas, and its potential as a fractured carbonate hydrocarbon reservoir: M.S. Thesis, Texas A&M University–Kingsville, 352 p.

Petzet, G. A., 1990, Buda strikes may boost South Texas action: Oil and Gas Journal, v. 88, no. 20, <https://www.ogj.com/articles/print/volume-88/issue-20/in-this-issue/exploration/buda-strikes-may-boost-south-texas-action.html>.

Phelps, R. M., C. Kerans, R. G. Loucks, R. Da-Gama, J. Jeremiah, and D. Hall, 2013, Oceanographic and eustatic control of carbonate platform evolution and sequence stratigraphy on the Cretaceous (Valanginian-Campanian) passive margin, northern Gulf of Mexico: Sedimentology, v. 62, 461–496, <https://doi.org/10.1111/sed.12062>.

Reaser, D. F., and W. C. Dawson, 1995, Geologic study of Upper Cretaceous (Cenomanian) Buda Limestone in northeast Texas with analysis of some regional implications: Gulf Coast Association of Geological Societies Transactions, v. 45, 495–502.

Savrda, C. E., J. V. Browning, H. Krawinkel, and S. P. Hesselbo, 2001, Firmground ichnofabrics in deep-water sequence stratigraphy, Tertiary clinoform-toe deposits, New Jersey slope: *Palaios*, v. 15, p. 294–305, <https://doi.org/10.1669/0883-1351(2001)016<0294:FIIDWS>2.0.CO;2>.

Scott, R. J., 1977, The Austin Chalk–Buda trend of South Texas: Gulf Coast Association of Geological Societies Transactions, v. 27, p. 164–168.

Smirnov, A., and C. L. Liner, 2018, Interpretation and fracture characterization of Upper Cretaceous Buda Limestone Formation using post-stack 3D seismic data in Zavala County, Texas: American Association of Petroleum Geologists Search and Discovery Article 11108, Tulsa, Oklahoma, 20 p., <http://www.searchanddiscovery.com/documents/2018/11108smirnov/ndx_smirnov.pdf> Accessed November 5, 2018.

Snyder, R. H., and M. Craft, 1977, Evaluation of Austin and Buda Formations from core and fracture analysis: Gulf Coast Association of Geological Societies Transactions, v. 27, p. 376–385.

Stapp, W. L., 1977, The geology of the fractured Austin and Buda formations in the subsurface of South Texas: Gulf Coast Association of Geological Societies Transactions, v. 27, p. 208–229.

Stow, D. A. V., J. C. Faugères, A. Viana, and E. Gonthier, 1998, Fossil contourites: A critical review: Sedimentary Geology, v. 115, p. 3–31, <https://doi.org/10.1016/S0037-0738(97)00085-7>.

van der Molen, 2004, Sedimentary development, seismic stratigraphy and burial compaction of the Chalk Group in the Netherlands North Sea area: Ph.D. Dissertation, Utrecht University, Netherlands, 175 p.

Zahm, C. K., and M. Enderlin, 2010, Characterization of rock strength in Cretaceous strata along the Stuart City Trend, Texas: Gulf Coast Association of Geological Societies Transactions, v. 60, p. 693–702.

Zahm, C. K., and C. Kerans, 2012, The use of stratigraphic architecture and rock strength for improved carbonate fractured reservoir modeling—Examples form outcrop analogs and subsurface reservoirs: American Association of Petroleum Geologists Search and Discovery Article 120097, Tulsa, Oklahoma, 13 p., <http://www.searchanddiscovery.com/documents/2012/120097zahm/ndx_zahm.pdf>.

Zahm, C. K., R. G. Loucks, and B. G. Gates, 2019, High-resolution rock strength and the implications for reservoir geomechanics in the Cenomanian-age Buda Formation, Dimmit County, Texas: Gulf Coast Association of Geological Societies Journal, v. 8, p. 268–280, <https://www.gcags.org/Journal/2019.GCAGS.Journal/2019.GCAGS.Journal.v8.14.p268-280.Loucks.et.al.pdf>.